Research Square

Preprints are preliminary reports that have not undergone peer review.
They should not be considered conclusive, used to inform clinical practice,
or referenced by the media as validated information.

Mesenchymal drift in skeletal muscle drives bone loss via secretome remodeling and is attenuated by partial reprogramming

Min Ma

drmamin@163.com

Department of Joint Surgery, Shanghai East Hospital, School of Medicine, Tongji University

Mingchong Liu

Department of Traumatic Surgery, Shanghai East Hospital, School of Medicine, Tongji University, Shanghai 200092, China.

Jingyi Wang

Department of Joint Surgery, Shanghai East Hospital, School of Medicine, Tongji University

Zhiying Pang

Translational Stem Cell Research Center, Dongfang Hospital, School of Medicine, Tongji University, Shanghai, China.

Aoyuan Fan

Department of Joint Surgery, Shanghai East Hospital, School of Medicine, Tongji University

Zhiqiang Gao

Department of Joint Surgery, Shanghai East Hospital, School of Medicine, Tongji University

Chensong Yang

Department of Traumatic Surgery, Shanghai East Hospital, School of Medicine, Tongji University, Shanghai 200092, China.

Changqing Ai

Department of Traumatic Surgery, Shanghai East Hospital, School of Medicine, Tongji University, Shanghai 200092, China.

Xiaoyu Cai

Department of Spine Surgery, The First Affiliated Hospital of Xinjiang Medical University, Urumqi, China

Yuhang Qiao

Department of Bone Tumor, The First Affiliated Hospital of Xinjiang Medical University, Urumqi, Xinjiang, China

Laiya Lu

Department of Traumatic Surgery, Shanghai East Hospital, School of Medicine, Tongji University, Shanghai 200092, China.

Ming Xia

Department of Orthopaedics, Shanghai Tenth People's Hospital, School of Medicine, Tongji University, Shanghai 200072, China.

Shulin Luo

Department of Joint Surgery, Shanghai East Hospital, School of Medicine, Tongji University

Feng Yin

Tongji University https://orcid.org/0000-0002-2070-0085

Article

Keywords: Mesenchymal drift, Skeletal muscle, Muscle secretome, Partial reprogramming, Bone metabolism

Posted Date: November 19th, 2026

DOI: https://doi.org/10.21203/rs.3.rs-11476768/v1

License: This work is licensed under a Creative Commons Attribution 4.0 International License. Read Full License

Additional Declarations: There is **NO** Competing Interest.

Mesenchymal drift in skeletal muscle drives bone loss via secretome remodeling and is attenuated by partial reprogramming

Mingchong Liu[1,2#], Jingyi Wang[1#], Zhiying Pang[1#], Aoyuan Fan[1], Zhiqiang Gao[1], Chensong Yang[2], Changqing Ai[2], Xiaoyu Cai[3], Yuhang Qiao[4], Laiya Lu[2], Ming Xia[5], Shulin Luo[1#], Feng Yin[1,2*], Min Ma[1*]

1 Department of Joint Surgery, Shanghai East Hospital, School of Medicine, Tongji University, Shanghai 200092, China.

2 Department of Traumatic Surgery, Shanghai East Hospital, School of Medicine, Tongji University, Shanghai 200092, China.

3 Department of Spine Surgery, The First Affiliated Hospital of Xinjiang Medical University, Urumqi, China

4 Department of Bone Tumor, The First Affiliated Hospital of Xinjiang Medical University, Urumqi, Xinjiang, China

5 Department of Orthopaedics, Shanghai Tenth People's Hospital, School of Medicine, Tongji University, Shanghai 200072, China.

*Correspondence:

Shulin Luo: 18502116399@163.com

Feng Yin: yinfeng001@sina.com

Min Ma: drmamin@163.com

# Mingchong Liu, Jingyi Wang, and Zhiying Pang contributed equally to this work.

Abstract

Aging is an intricate systemic process profoundly influenced by inter-organ communication, where skeletal muscle functions as a major endocrine hub. Here, we identify mesenchymal drift (MD) as a conserved transcriptomic and structural hallmark of aged skeletal muscle across human and mice cohorts. MD drives a hyper-secretory phenotype, triggering the excessive release of pro-inflammatory myokines and extracellular vesicles (EVs). Localized in vivo partial reprogramming (OSK) of aged muscle successfully attenuates local MD, rejuvenates the aberrant secretome, restores

skeletal muscle mass and function, rescues age-related bone loss, and partially alleviates aging phenotypes in a subset of distant organs. Through functional add-back interventions, we mechanistically decouple cell-autonomous muscle rejuvenation from the secretome-dependent partial amelioration of distant organ senescence. Furthermore, single-cell transcriptomics and in vivo profiling pinpoint an expanding subpopulation of $EGFR^+$ fibro-adipogenic progenitors (FAPs) as the principal cellular drivers of both MD and the aging secretome. Finally, utilizing engineered anti-PDGFRα-targeted lipid nanoparticles (LNPs) to deliver OSK mRNA or EGFR siRNA exclusively to FAPs, we successfully suppress the hyper-secretory phenotype, reverse osteoporotic decline, and partly mitigate distal organ aging. Together, our findings establish MD-driven secretome remodeling as a pivotal governor of systemic aging and present a highly translatable, FAP-targeted nanomedical strategy for organismal rejuvenation.

Keywords: Mesenchymal drift; Skeletal muscle; Muscle secretome; Partial reprogramming; Bone metabolism.

Introduction:

Aging is an intricate, systemic process characterized by the synchronous functional decline of multiple organ systems (1). The emergence of concepts such as inflammaging and immunosenescence highlights that the pathogenesis of aging is largely driven by holistic, systemic alterations rather than isolated local defects (2-4). Viewing aging through a macro-systemic lens may provide a higher-dimensional framework to decode its underlying biological mechanisms. Beyond the canonical central regulation orchestrated by the nervous, endocrine, and immune systems, peripheral organs actively participate in maintaining organismal homeostasis via complex autocrine, paracrine, and endocrine cross-talk (5-8). Notably, skeletal muscle, which constitutes the largest mass of any organ in the human body, exerts profound systemic endocrine effects (9-11). This paradigm is strongly supported by fundamental research delineating cross-organ communication networks such as the muscle-bone, muscle-brain, and muscle-liver and muscle-gut axes, as well as by clinical observations linking sarcopenia with multi-systemic comorbidities, including osteoporosis and Alzheimer's disease (12-20).

The endocrine function of skeletal muscle is primarily mediated by myokines, a diverse repertoire of soluble proteins and exosome-encapsulated factors that exert distant pleiotropic effects on bone, brain, and adipose tissue (11, 19, 21-23). Well-characterized myokines, including IL-6, FGF21, IL-33, and CX3CL1, often function dually as classic cytokines and established markers of inflammaging (18, 20, 22, 24-27). Intriguingly, these factors also heavily overlap with the senescence-associated secretory phenotype (SASP), functionally converging the skeletal muscle secretome with the broader biology of organismal aging (8, 28). During the aging process, skeletal muscle progressively adopts a hyper-secretory phenotype, dominated by the excessive release of pro-inflammatory factors (29, 30). Upon entering the systemic circulation, these factors may actively drive systemic chronic inflammation, exacerbating inflammaging and ultimately accelerating systemic decline (3, 31, 32). This dynamic presents a compelling biological premise: targeted rejuvenation of the local skeletal muscle secretome may serve as a viable strategy to partially counteract the trajectory of systemic aging.

To elucidate the regulatory mechanisms governing the skeletal muscle secretome, we turned to the emerging concept of mesenchymal drift (MD) (33). MD is a cellular identity shift phenotypically characterized by altered extracellular matrix (ECM) production, disruption of cellular junctions, tissue mechanical stiffening, and aberrant cytokine production (33, 34). These pathological features strikingly mirror the age-related secretory dysregulation observed in skeletal muscle, suggesting that MD may serve as a pivotal hallmark and core driver of this secretory shift. Consequently, we hypothesized that age-related MD orchestrates the detrimental alterations in the muscle secretome.

In this study, we provide comprehensive evidence validating this hypothesis. Through the analysis of extensive human cohorts, we identified that MD is a prominent and conserved feature of aged human skeletal muscle. In aged mice models, targeted local partial reprogramming of skeletal muscle successfully rejuvenated the myokine secretome. This localized intervention subsequently rescued bone loss, the physiological parameter most strictly coupled with muscle endocrine function, and partly alleviated systemic aging phenotypes. Crucially, analyzing single-cell RNA sequencing (scRNA-seq) data, we pinpointed a distinct subpopulation of EGFR+ fibro-adipogenic progenitors (FAPs) as the primary cellular effectors driving skeletal muscle MD. Targeted ablation or molecular regulation of FAPs robustly attenuated muscle MD, restored a youthful secretory profile, and alleviated aging phenotypes in a subset of remote organs. Together, our findings elucidate a novel mechanistic paradigm wherein localized muscle MD dictates systemic aging, and establish the targeted rejuvenation of the skeletal muscle secretome as a viable, highly translational therapeutic strategy for age-related systemic decline.

Methods:

Gene sets and transcriptomic signatures

To systematically evaluate the transcriptional dynamics of mesenchymal drift (MD) and its impact on the skeletal muscle secretome, we curated specific gene signatures from publicly available databases and previously published studies. The MD gene signature was directly derived from previously established and published datasets (35). A consensus myokine signature was constructed by aggregating functionally validated myokines consistently reported in prior literature. To interrogate the intracellular machinery governing secretory phenotypes, ontology-based gene sets were extracted from the Gene Ontology (GO) database. These specific terms encompassed: Extracellular Vesicle Biogenesis (GO:0140112), Vesicle-mediated Transport (GO:0016192), Extracellular Exosome Assembly (GO:0071971), and Secretory Vesicle (GO:0099503). To account for inherent differences in gene composition between human and mice genomes, species-specific versions of each gene set were utilized. A comprehensive compendium of all utilized gene sets, including species-specific gene lists, GO accession identifiers, and original literature sources, is provided in Supplementary Table 1.

Gene expression analyses and gene set enrichment analysis

To quantitatively evaluate the transcriptional burden of mesenchymal drift (MD), we employed a dual-analytical strategy based on established theoretical frameworks (35). First, the baseline MD activity for individual samples was determined by computing the median expression value across all constituent genes within the MD signature. For these calculations, transcript abundances were measured as transcripts per million (TPM) in RNA-seq cohorts, whereas normalized signal intensities were utilized for microarray-

based datasets. Second, Gene Set Enrichment Analysis (GSEA) was independently applied to assess the global enrichment topology of the MD pathway. The evaluation of all other curated transcriptomic signatures was conducted exclusively via GSEA to determine their normalized enrichment scores. For the assessment of individual gene expression profiles, transcript levels were represented using platform-appropriate metrics (TPM for RNA-seq and normalized intensities for microarrays). Furthermore, to ascertain statistical dependencies among continuous variables, individual gene expression levels, and aggregated pathway scores, non-parametric Spearman's rank correlation analyses were systematically performed.

Bulk RNA sequencing

Total RNA was extracted from harvested skeletal muscle tissues using TRIzol reagent (Invitrogen, USA) following immediate mechanical tissue homogenization. RNA yield and purity were spectrophotometrically evaluated via a NanoDrop 2000 (Thermo Fisher Scientific, USA), and RNA integrity was rigorously verified using an Agilent 2100 Bioanalyzer (Agilent Technologies, USA). Sequencing libraries were prepared utilizing the VAHTS Universal V6 RNA-seq Library Prep Kit strictly according to the manufacturer's protocols. Subsequent high-throughput sequencing was executed on an Illumina NovaSeq 6000 platform to generate 150-bp paired-end reads. For the bioinformatic processing pipeline, raw sequencing data were subjected to quality control using fastp to trim adapter sequences and eliminate low-quality reads. The resultant high-fidelity reads were aligned to the respective reference genome utilizing the HISAT2 aligner. Read mapping and counting at the gene level were performed with HTSeq-count. Raw read counts were subsequently normalized to transcripts per million (TPM) to establish expression abundance and facilitate downstream quantitative analyses.

Datasets

Publicly available human skeletal muscle bulk RNA-sequencing (bulk RNA-seq) datasets were retrieved from the Gene Expression Omnibus (GEO) database. Filtering for the availability of clinical annotations resulted in the final inclusion of 29 independent datasets to evaluate the effects of mesenchymal drift (MD). Detailed characteristics, sample sizes, and clinical metadata for all 29 human cohorts are summarized in Supplementary Table 2.

Mice

All animal procedures were conducted in strict compliance with ethical regulations and were approved by the Institutional Animal Care and Use Committee of Shanghai East Hospital (2024 animal research review No. 152). Mice were housed in a specific pathogen-free (SPF) facility maintained under a standard 12 hr light/12 hr dark cycle, with tightly controlled ambient temperature and humidity. All animals were provided ad

libitum access to standard laboratory chow and water. For aging-associated comparative models, young and older mice cohorts were strictly defined as 4 months and 20 months of age, respectively, at the initiation of the experimental procedures.

To restrict therapeutic modulation to the local skeletal muscle microenvironment and circumvent systemic off-target effects, all biological agents were administered strictly via targeted localized intramuscular (i.m.) injections. For intervention paradigms, a 12-week treatment cycle was established. Within this framework, adeno-associated virus (AAV) vectors were delivered once every 4 weeks. Recombinant myokine cocktails were administered daily, with the dosage precisely calibrated to 1 μg/kg of body weight for each individual myokine component. Purified extracellular vesicles (EVs) were locally injected every 3 days at a standardized dose of 25 μg per administration (30). Upon completion of the 12-week regimen, animals were humanely euthanized for immediate skeletal muscle procurement. For transcriptional modulation paradigms utilizing lipid nanoparticle delivery systems, liposome-encapsulated nucleic acids were administered via i.m. injection every 3 days. Dosing was standardized to an equivalent of 10 μg/dose for siRNAs and 20 μg/dose for mRNAs. To assess acute molecular responses, animals in the liposomal cohorts were euthanized and tissues were harvested strictly following a total of three consecutive injections.

Enzyme-linked immunosorbent assay (ELISA)

To quantitatively profile the skeletal muscle secretome and specific systemic cytokine fluctuations, protein concentrations across diverse tissues and cellular fractions were systematically determined via Enzyme-Linked Immunosorbent Assays (ELISAs). Sample procurement, encompassing the immediate harvesting and mechanical homogenization of specific organs, alongside the collection of in vitro cell culture samples, was executed strictly following the manufacturer's standardized preparation protocols. The quantitative detection of targeted circulating and tissue-resident factors was performed using a comprehensive panel of highly specific, commercially available mice ELISA kits: IGF-2 (Cat# JL10182), bFGF (Cat# JL10364), OPG (Cat# JL10935), IL-1β (Cat# JL18442), CX3CL1 (Cat# JL20148), IL-15 (Cat# JL20248), IL-17A (Cat# JL20251), IL-6 (Cat# JL20268), Myostatin (Cat# JL20385), MMP-2 (Cat# JL20388), FGF21 (Cat# JL22924), FSTL1 (Cat# JL28982), GDF11 (Cat# JL31603), and Musclin (Cat# JL58270), all procured from JonlnBio (Shanghai, China). All microplate incubations, washings, and colorimetric development steps were processed rigorously according to the supplier's specific instructions. Final absolute analyte concentrations were extrapolated from rigorously validated, assay-specific standard curves generated concurrently with the experimental samples.

RNA extraction and real-time PCR

Total RNA was efficiently isolated from harvested biological specimens—encompassing both homogenized tissue samples and in vitro cell cultures, utilizing the RNAeasy™ Animal RNA Isolation Kit equipped with spin columns (Cat# R0026, Beyotime) in strict adherence to the manufacturer's standardized protocols. The absolute yield and spectrophotometric purity of the resulting RNA preparations were rigorously verified utilizing a NanoDrop 2000 spectrophotometer (Thermo Fisher Scientific, USA). For template generation, first-strand cDNA synthesis was executed using the PrimeScript RT Master Mix (Cat# RR036Q, TaKaRa, Japan).Quantitative real-time PCR was deployed to systematically interrogate the transcriptional dynamics of key biological modules central to this study. The comprehensive transcriptomic panel encompassed: Oct4, Sox2, Klf4, Cdkn1a, Cdkn2a, Fgf21, Cx3cl1, Mstn, Il6, Ccl2, Cxcl2, Cxcl10, Il1a, Il1b, Mmp3, Tnf, Col1a1, Col3a1, Col4a1, Timp2, Timp3, Mmp14, Ocn, Col1a, Alp, Runx2, and Egfr. Additionally, to evaluate cellular aging at the chromosomal level, relative telomere length was independently quantified via real-time PCR utilizing matched genomic DNA extracts. All amplification procedures were conducted on a high-throughput real-time PCR platform. The thermocycling parameters were meticulously standardized, consisting of an initial template denaturation phase, followed by 40 amplification cycles of denaturation at 95°C for 15 s and a combined optimal annealing/extension step at 60°C for 1 min. To ensure technical reproducibility and statistical robustness, all target quantifications were performed in independent triplicates (n = 3). Relative transcript abundances and telomere lengths were computationally derived utilizing the $2^{-\Delta\Delta Ct}$ methodology. The primer sequences deployed in these analyses are provided in Supplementary Table 3.

Western blot

Total proteins from skeletal muscle tissues, isolated EVs, and cell lysates were extracted utilizing RIPA buffer supplemented with protease and phosphatase inhibitors. Protein concentrations were quantified and normalized via a BCA protein assay. Equivalent amounts of denatured protein lysates were resolved by SDS-PAGE and electro-transferred onto PVDF membranes. After blocking with 5% non-fat dry milk or BSA in TBST, membranes were probed overnight at 4°C with specific primary antibodies against EGFR, CD9, CD63, TSG101, RAB27A, and GAPDH. Following subsequent incubation with corresponding HRP-conjugated secondary antibodies, immunoreactive bands were visualized utilizing an enhanced chemiluminescence (ECL) system. Digital densitometric quantification was performed via ImageJ, with the expression levels of all target proteins strictly normalized to the endogenous GAPDH loading control.

Histology and Immunostaining

Harvested skeletal muscles and femurs were fixed in 4% paraformaldehyde, with femurs undergoing extensive decalcification prior to standard paraffin embedding and sectioning.

For all immunostaining procedures, tissue sections were subjected to standard antigen retrieval and blocking before primary antibody incubation.

For skeletal muscle analyses, general morphology was evaluated utilizing standard hematoxylin and eosin (H&E) staining. Immunohistochemistry (IHC) was performed for p21 and RAB27A. Immunofluorescence (IF) staining was conducted for p16. Additionally, multiplex IF was executed on skeletal muscle sections to specifically co-stain for LAMININ/RAB27A and EGFP/LAMININ/OCT4/KLF4.

For femoral analyses, Masson's trichrome and tartrate-resistant acid phosphatase (TRAP) staining were executed. Immunostaining procedures for femoral sections included the detection of COL-1 (evaluated via both IHC and IF modalities) and OCN.

Following overnight incubation at 4°C with primary antibodies, sections were incubated with appropriate species-matched fluorophore- or horseradish peroxidase (HRP)-conjugated secondary antibodies. Histological and fluorescent signals were acquired utilizing a slide-scanning or confocal microscope. All downstream morphological and fluorescence intensity quantifications were systematically processed using ImageJ software.

Extracellular vesicles (EVs) isolation and characterization

Extracellular vesicles (EVs) were isolated from mice skeletal muscle tissues, cell culture supernatants, and serum utilizing a standardized differential ultracentrifugation protocol. For tissue-derived EVs, fresh skeletal muscles were minced and enzymatically digested with collagenase D (2 mg/mL) and DNase I (40 U/mL) in DMEM for 30 min at 37°C under gentle agitation. The resulting tissue suspensions were passed through a 70-μm cell strainer. For in vitro EV collection, primary fibro-adipogenic progenitors (FAPs) were cultured in DMEM supplemented with 10% EV-depleted FBS (NEWZERUM) or EBSS.

To purify EVs, the tissue digests and conditioned media were subjected to sequential centrifugation at 4°C: 300 × g for 10 min and 2,000 × g for 20 min to deplete cells and apoptotic debris, followed by 10,000 × g for 30 min to remove large microvesicles and organelles. The clarified supernatants were filtered through a 0.22-μm membrane and ultracentrifuged at 100,000 × g for 70 min at 4°C utilizing a Beckman Coulter Optima ultracentrifuge equipped with a Type 70 Ti rotor. The resulting EV pellets were washed in sterile PBS and subjected to a second ultracentrifugation step at 100,000 × g for an additional 70 min. The final purified EV pellets were resuspended in PBS for immediate downstream application or characterization.

To authenticate EV identity and purity, multiparametric characterization was performed. Vesicle morphology and ultrastructure were directly visualized via transmission electron microscopy (TEM). Particle size distribution and absolute EV concentrations were quantitatively profiled utilizing Nanoparticle Tracking Analysis (NTA). Furthermore, the

robust enrichment of canonical EV-specific biogenesis markers and tetraspanins, specifically CD9, CD63, and TSG101, was independently validated via immunoblotting as described in the protein analysis section.

AAV construction and administration

Adeno-associated virus serotype 9 (AAV9) vectors were utilized to achieve highly efficient localized transduction in skeletal muscle. A polycistronic AAV9-OSK vector was engineered to concurrently express mice Oct4, Sox2, and Klf4 under the control of the elongation factor-1 alpha short (EFS) promoter, seamlessly linked by self-cleaving 2A peptides (Oct4-P2A-Sox2-T2A-Klf4). Corresponding AAV9 vectors driving enhanced green fluorescent protein (AAV-EGFP) or carrying a non-coding sequence (AAV-CT) under identical regulatory elements served as experimental controls. All viral constructs were commercially synthesized, packaged, and rigorously titered (>1 × 10^{12} genome copies/mL via qPCR) by Haixing Biosciences (Shanghai, China). Detailed parameters for in vivo localized intramuscular administration are delineated in the targeted delivery section above.

Muscle Functional and Morphometric Analysis

To evaluate skeletal muscle macro-morphometry, the absolute masses of the isolated gastrocnemius (GA) and quadriceps (QU) were systematically recorded and strictly normalized to total body weight to derive specific muscle indices (GA/body weight and QU/body weight). Micro-anatomical morphometry, specifically the mean myofiber cross-sectional area (CSA), was quantitatively delineated from standardized histological sections using ImageJ.

Systemic exercise endurance was evaluated utilizing a motorized treadmill platform (LE8710MTS, Harvard Apparatus). Following a two-day familiarization protocol (10 cm/s for 5 min/day), mice were subjected to a progressive uphill (15° incline) endurance test. The initial running velocity was established at 10 cm/s, with stepwise increments of 5 cm/s every 4 min. Exhaustion was strictly defined as the physiological inability to maintain locomotion, objectively marked by >10 s of continuous contact with the posterior electrical grid. Total exhaustion time (min) and cumulative distance traversed (m) were autonomously acquired via SeDaCOM v2.0 software.

Furthermore, in vivo muscle contractility was interrogated utilizing an intact muscle test system (Aurora Scientific). Under continuous 2% isoflurane anesthesia, maximal plantarflexion tetanic torque was elicited via supramaximal electrical stimulation of the tibial nerve (150 Hz frequency, 0.2 ms pulse duration). Contractile dynamics were recorded using DMA v5.501 software and subsequently normalized to corresponding muscle mass to yield specific tetanic torque (mN·m/g), ensuring accurate evaluation of intrinsic muscle quality independent of gross muscle volume.

Mitochondrial respiration

Functionally intact mitochondria were isolated from freshly harvested organs and tissues utilizing the Mitochondria Isolation Kit (Cat# 89801, Thermo Fisher Scientific). The oxygen consumption rate (OCR) of the isolated mitochondrial fractions was quantitatively profiled in mitochondrial assay solution utilizing the Seahorse XF Mito Stress Test Kit (Cat# 103015-100, Agilent Technologies).

Micro-CT

Following the 12-week experimental paradigm, harvested mice femurs were subjected to high-resolution micro-computed tomography Micro-CT) utilizing a Quantum GX imaging system (PerkinElmer) in strict adherence to the American Society for Bone and Mineral Research (ASBMR) guidelines. Three-dimensional architectural reconstructions and downstream quantitative morphometric analyses were systematically executed utilizing NRecon and CTAn software suites (Bruker), respectively. To ensure anatomical consistency across all experimental cohorts, the region of interest (ROI) was rigorously delineated, commencing immediately adjacent to the distal femoral growth plate and extending exactly 2 mm proximally into the metaphysis. Within this standardized volumetric space, critical trabecular and cortical bone indices were quantitatively derived, encompassing bone volume fraction (BV/TV), trabecular thickness (Tb.Th), trabecular number (Tb.N), and trabecular separation (Tb.Sp).

Biomechanical analysis

Mouse femurs were subjected to a 3-point bending test utilizing an Instron 3366 Universal Testing System (Instron). Femurs were positioned on a standardized support fixture, and mechanical loading was applied to the mid-diaphysis at a constant displacement rate of 2 mm/min until fracture. Biomechanical and material parameters were directly calculated from the resulting load-displacement curves, specifically including ultimate stress (MPa), elastic modulus (MPa), and stiffness (N/mm).

Single-cell sequencing data analysis

Publicly available single-cell RNA-sequencing (scRNA-seq) datasets (GEO: GSE167186 and GSE268953) were acquired for transcriptomic profiling. Primary data quality control, normalization, dimensionality reduction, and initial unsupervised clustering for core cell type annotation were executed strictly conforming to the standardized bioinformatic pipelines delineated in their respective original source publications. For targeted high-resolution analysis, the identified cellular populations were subsequently isolated, sub-clustered, and meticulously stratified based on the quantitative expression profiles of the mesenchymal drift (MD) transcriptional signature.

To systematically evaluate aging-driven microenvironmental and transcriptomic alterations, algorithmic MD module scores, absolute expression levels of individual secretome-associated genes, and aggregate secretory gene set activities were quantitatively compared between the young and aged cohorts. Functional enrichment analysis of differentially expressed features was systematically performed utilizing the Gene Ontology (GO) database to elucidate underlying biological processes and pathway shifts. All core computational clustering, scoring, and visualization procedures were executed within the R statistical environment utilizing the Seurat package.

Flow cytometry and fluorescence-activated cell sorting (FACS)

Skeletal muscles harvested from mice were minced and subjected to sequential enzymatic digestion utilizing collagenase type II, followed by a combination of collagenase D (Roche) and dispase II (Roche) at 37°C. The generated single-cell suspensions were serially filtered through 100-μm and 40-μm strainers, and erythrocytes were effectively depleted using a standard red blood cell lysis buffer. Following resuspension in a wash buffer (PBS supplemented with 2% FBS), the mononuclear cells were incubated at 4°C in the dark with a custom fluorophore-conjugated primary antibody cocktail.

To specifically identify and isolate the target $EGFR^+$ fibro-adipogenic progenitor (FAP) or total FAPs subpopulation, cells were rigorously sorted based on the surface signature profile: Integrin $\alpha7^-$, $CD31^-$, $CD45^-$, $Sca\text{-}1^+$, and $EGFR^+$ (for total FAPs: Integrin $\alpha7^-$, $CD31^-$, $CD45^-$, and $Sca\text{-}1^+$) (36). The specific targeted labeling panel comprised FITC-conjugated antibodies against Integrin α7, CD31, and CD45, combined with PE-conjugated anti-Sca-1 and APC-conjugated anti-EGFR. Target cell sorting was executed utilizing a BD FACSAria III cell sorter (BD Biosciences). Routine analytical flow cytometry was conducted on a BD FACSCalibur, with all downstream data visualization and gating strategies systematically processed via FlowJo v10 software.

Cell culture procedure and treatment

To evaluate the activation dynamics of the EGFR signaling axis, primary fibro-adipogenic progenitors (FAPs) were independently stimulated with five distinct recombinant EGFR ligands: EGF, TGFA, BTC, AREG, and HBEGF. All ligands were uniformly administered at a standardized concentration of 100 ng/mL. For targeted pathway inhibition assays, FAPs were subjected to treatments with PBS (vehicle control), TGFA alone, or TGFA combined with the selective EGFR tyrosine kinase inhibitor gefitinib (5 μM). Following these specific pharmacological interventions, the treated FAPs were established in an in vitro co-culture system with an osteoblast cell line. Furthermore, to interrogate the interplay between local receptor activation and transcriptional reprogramming, FAPs were initially stimulated with TGFA and subsequently transduced with specific viral vectors: AAV-CT, AAV-OSK, or AAV-OSK combined with an EGFR overexpression construct (EGFR-OE). Following successful

viral transduction, these engineered FAPs were analogously subjected to co-culture with the osteoblast cell line for downstream functional evaluations.

Cell transfection

To construct the EGFR overexpression (EGFR-OE) plasmid, the full-length coding sequence of the mouse Egfr gene was amplified and cloned into a standard pcDNA3.1 mammalian expression vector. A corresponding empty pcDNA3.1 vector served as the negative control. For in vitro transient transfection, primary fibro-adipogenic progenitors (FAPs) were seeded to achieve 70-80% confluence and transfected with the designated plasmids utilizing Lipofectamine 3000 reagent (Invitrogen) in Opti-MEM reduced serum medium (Gibco). The transfection complexes were removed and replaced with standard complete culture media 6 hours post-transfection. Transfected cells were subsequently cultured for 48 hours prior to baseline expression validation or integration into the osteoblast co-culture system.

Cellular Staining Assays

To evaluate osteogenic differentiation and matrix mineralization, osteoblasts from the co-culture system were fixed in 4% paraformaldehyde (PFA) and subjected to Alkaline Phosphatase (ALP) and Alizarin Red S (ARS) staining. For phenotypic characterization, FAPs were fixed in 4% PFA, permeabilized with 0.1% Triton X-100, and blocked with 5% bovine serum albumin (BSA). The FAPs were incubated with a primary antibody against α-SMA, followed by a corresponding fluorophore-conjugated secondary antibody. Nuclei were counterstained with DAPI. Bright-field and immunofluorescence imaging were performed utilizing an inverted fluorescence microscope.

Liposome Preparation

Lipid nanoparticles (LNPs) were formulated utilizing a standardized microfluidic mixing protocol. The lipid organic phase, comprising the ionizable lipid, cholesterol, and DMG-PEG2000 at a molar ratio of 30:54.5:2, was prepared in absolute ethanol. Concurrently, OSK mRNA or EGFR siRNA was dissolved in 25 mM sodium acetate buffer (pH 5.2). The aqueous nucleic acid phase and the lipid organic phase were rapidly mixed through a microfluidic device at a 3:1 volume ratio and a total flow rate of 4 mL/min. The newly formed core nanoparticles (LNP@OSK mRNA and LNP@EGFR siRNA) were extensively dialyzed against PBS at 4°C to remove residual ethanol. To confer cellular targeting capabilities, anti-PDGFRα antibodies were mildly thiolated utilizing Traut's reagent and subsequently conjugated to DSPE-PEG2000-Maleimide via a stable thioether linkage to generate DSPE-PEG2000-anti-PDGFRα. These functionalized antibody-lipid conjugates were then co-incubated with the pre-formed LNPs at 37°C for 45-60 min. This process facilitated the spontaneous integration of the hydrophobic DSPE anchoring tails into the outer lipid layer of the LNPs. The final targeted nanoparticle assemblies (anti-

PDGFRα-LNP@OSK mRNA and anti-PDGFRα-LNP@EGFR siRNA) were purified via 100 kDa ultrafiltration to eliminate unconjugated components prior to downstream applications.

Statistical Analysis

All statistical analyses were executed within the R statistical computing environment. The Shapiro-Wilk test was employed to ascertain data normality. Continuous variables are presented as mean ± standard deviation (SD), and categorical variables are expressed as counts (percentages). For normally distributed continuous data, two-group and multi-group comparisons were evaluated utilizing independent Student's t-tests and one-way ANOVA followed by Tukey's post hoc test, respectively. For non-normally distributed data, the Wilcoxon rank-sum test (for two groups) or the Kruskal-Wallis test followed by Dunn's multiple comparisons test (for multiple groups) was applied. Categorical variables were analyzed via Chi-square or Fisher's exact tests, as dictated by sample size. Bivariate correlation analyses were performed utilizing Spearman's rank correlation coefficient.

Results:

MD in Skeletal Muscle is a Prevalent Hallmark of Aging and Muscle status in Human

To systematically interrogate the prevalence and distributional dynamics of skeletal muscle mesenchymal drift (MD) across human populations, we conducted a comprehensive transcriptomic screening of publicly available skeletal muscle datasets from the Gene Expression Omnibus (GEO). Following rigorous filtering to exclude datasets with incomplete clinical metadata or irrelevant experimental designs, we included 29 independent bulk RNA datasets encompassing both microarray and high-throughput RNA-seq platforms. This aggregated cohort totaled 1,797 samples from 1,188 individuals, representing a diverse array of ethnicities and demographics.

Broadly, across the vast majority of the analyzed datasets, aged individuals exhibited elevated baseline MD levels compared to their younger counterparts, with most comparisons reaching statistical significance ($p < 0.05$). Consistent with our established bioinformatic framework, we quantified MD utilizing two distinct metrics: median MD gene expression, which reflects the baseline transcriptional burden, and the Gene Set Enrichment Analysis (GSEA)-derived MD score, which captures global pathway enrichment. In the GSE28422 cohort (16 young and 12 older individuals), the older group demonstrated significantly higher levels of both median MD gene expression and MD scores compared to the young group (37)(Figure 1A). Similarly, in GSE97084 (29 young and 23 older individuals), older subjects maintained significantly elevated MD levels both before and after a 12-week training intervention, a pattern consistent across both

measurement modalities (38)(Figure 1B). Interestingly, in the GSE249921 dataset (30 young and 50 older individuals undergoing an acute bout of exercise, sampled at baseline, 3 hours, and 48 hours post-exercise), baseline MD levels were significantly higher in the older cohort (39)(Figure 1C). However, this age-related difference was blunted and no longer statistically significant following acute exercise (Figure S1A). This specific discrepancy between GSE249921 and GSE97084 implies that differing exercise modalities may exert heterogeneous effects on the dynamic regulation of the MD signature. The robust positive correlation between chronological age and MD was further corroborated in GSE242202 (40)(22 young and 37 older individuals) (Figure 1D, Figure S1B). A multitude of additional datasets consistently mirrored this trend, revealing significantly elevated MD levels in older populations and positive correlations between advancing age and MD activity (Figure 1E, Figure S1C–E). Notably, even in subsets where the difference between young and old cohorts narrowly missed statistical significance, the older groups consistently trended toward higher overall MD scores (Figure S1E).

Beyond chronological aging, we investigated the relationship between the MD transcriptional signature and functional skeletal muscle status. In GSE167186 (41), an older cohort diagnosed with sarcopenia exhibited significantly elevated median MD gene expression compared to both healthy young and healthy older individuals, with MD scores following an identical trend (Figure 1F, Figure S1F). Utilizing the specific clinical annotations available in this dataset, correlation analyses revealed that elevated MD levels positively correlated with poorer muscle functional parameters, although some associations did not reach strict statistical significance (Figure S1G). This structure-function relationship was powerfully validated in the GSE144303 cohort (n = 80), where muscle MD levels exhibited a significant negative correlation with both mean and maximum grip strength, and a positive correlation with 400-meter walk time (42)(Figure S1H). These findings firmly establish that heightened MD is a reliable transcriptomic indicator of impaired physical performance.

To account for the impact of age-associated systemic comorbidities on the local muscle microenvironment, we evaluated patients with osteoarthritis (OA). Analysis of the GSE242202 dataset, stratified into healthy young (n = 15), young with OA (n = 7), and older adults with OA (n = 37), revealed that both young and aged OA patients displayed significantly higher median MD gene expression and MD scores compared to healthy young controls (Figure 1G, Figure S2A). This indicates that pathological joint microenvironments and systemic stress can prematurely drive skeletal muscle MD, independent of chronological aging alone.

We further explored the influence of physical exercise on skeletal muscle MD, noting considerable inter-study heterogeneity. In GSE151066 (43), which monitored 19 older patients undergoing an acute bout of cycling exercise, muscle MD levels spiked

significantly immediately post-exercise and remained elevated above baseline at the 3-hour mark (Figure 1H, Figure S2B). This acute induction was mirrored in GSE249921 following resistance exercise, where MD levels rose significantly at 3 hours and peaked at 48 hours relative to baseline (Figure 1I, Figure S2C). Conversely, acute exercise did not elicit a unified MD shift in GSE28422 (28 subjects undergoing 12-week resistance training). During the naive baseline acute bout (prior to the 12-week regimen), median MD gene expression paradoxically decreased 4 hours post-exercise, while the MD score remained statistically stable (Figure S2D). However, evaluating long-term adaptations in the same cohort, 12 weeks of resistance training fundamentally elevated baseline MD levels compared to pre-training states (Figure 1J, Figure S2E). This longitudinal elevation in MD subsequent to prolonged training was corroborated by GSE97084, suggesting that while the immediate acute response is highly modality-dependent, chronic exercise adaptation generally promotes an upregulation of the MD signature (Figure 1K, Figure S2F). It is worth noting, however, that findings from GSE1786 and GSE8479 did not distinctly support this long-term exercise-induced MD elevation, further highlighting the complex interplay between physical activity and local tissue state (Figure S2G, H).

Finally, we sought to examine the MD landscape at the extreme developmental spectrum of the human lifespan. Intriguingly, in dataset GSE4667 (comprising 4 pediatric and 5 elderly subjects), pediatric skeletal muscle exhibited significantly higher MD levels than that of the elderly adults (44)(Figure 1L, Figure S1I). This unexpected trend was further corroborated by GSE257558 (45), which compared skeletal muscle from young infants (7 to 28 months) with fully mature adults; infant tissues demonstrated substantially elevated MD levels relative to adult baselines (Figure 1L, Figure S1I). While seemingly paradoxical in the context of aging-associated decline, this phenomenon is likely attributable to the intrinsic composition of the MD gene signature. MD is phenotypically characterized by altered extracellular matrix (ECM) production, tissue remodeling, and shifts in cellular identity (33). During infancy and childhood, skeletal muscle undergoes rapid, physiological accretion of mass, necessitating dynamic ECM turnover, robust progenitor cell activation, and a highly plastic, mesenchymal-like state to accommodate developmental myofiber hypertrophy.

MD is Broadly Correlated with the Skeletal Muscle Secretome in Human

To comprehensively delineate the relationship between mesenchymal drift (MD) and the skeletal muscle secretome, we evaluated this functional interplay across two primary dimensions: the soluble repertoire of secreted proteins (myokines) and the extracellular vesicle (EV) secretory apparatus. Based on an extensive literature review, we curated a panel of 39 functionally validated myokines, aggregating them to construct a consensus "myokine signature". Concurrently, to capture the vesicular secretory dimension, we incorporated established ontology-based gene signatures derived from the Gene Ontology (GO) database. These specific functional modules included Extracellular Vesicle

Biogenesis, Vesicle-mediated Transport, Extracellular Exosome Assembly, and Secretory Vesicle.

We subsequently performed systematic correlation analyses between the transcriptomic signatures of these secretory pathways and MD levels across the diverse human meta-cohorts. Remarkably, in nearly all analyzed datasets, both the global MD scores (Figure 1M) and the baseline median MD gene expression levels (Figure S2J) exhibited a robust, highly significant positive correlation with the aforementioned secretome signatures. This widespread transcriptomic synchronization strongly indicates that an elevated MD burden is intrinsically linked to a hyper-secretory phenotype in human skeletal muscle, characterized by both amplified myokine production and enhanced EV output.

To further resolve this relationship at the individual transcript level, we conducted parallel correlation analyses mapping MD severity against the expression profiles of specific myokine genes. Consistent with our global signature enrichment findings, the transcriptional upregulation of numerous individual myokines demonstrated a striking positive correlation with local MD activity. This highly conserved dependency was consistently observed across the cohorts, regardless of whether the MD burden was quantified via the composite GSEA-derived MD score (Figure 1N) or the median expression of the constituent MD genes (Figure S2K).

Age-Dependent MD and the Skeletal Muscle Secretome Profile in Mice Models

To empirically validate the structural and transcriptomic phenomena observed in human cohorts, we translated our investigation to established in vivo mice aging models, utilizing cohorts strictly defined as 4 months (young) and 20 months (aged) of age. Consistent with our human data, the skeletal muscle of aged mice exhibited profoundly elevated MD levels compared to young controls (Figure 2A). Concurrently, we quantified gross muscle morphometry, including the absolute masses of the gastrocnemius (GA) and quadriceps (QU), alongside their specific muscle-to-body-weight indices. Expectedly, these critical indices of muscle mass demonstrated a robust negative correlation with local MD levels, reinforcing MD as a transcriptomic hallmark of muscle atrophy (Figure 2B, Figure S3A–C).

We next evaluated the local secretory landscape. The composite myokine signature was significantly upregulated in the aged mice muscle (Figure 2C). To achieve a higher molecular resolution, we performed correlation analyses between global MD levels and individual myokine transcripts. This revealed that the expression of multiple key myokines, specifically Cx3cl1, Fgf2, Fgf21, Fstl1, Gdf11, Igf2, Il15, Il17a, Il1b, Il6, Mmp2, Mstn, Ostn, and Tnfrsf11b, correlated significantly with MD burden, independent of whether MD was quantified via median expression or GSEA-derived scores (Figure 2D, Figure S3D). To translate these transcriptional changes into functional phenotypic outputs, we systematically determined the absolute protein concentrations of these

candidates in both local skeletal muscle tissue and systemic circulation via ELISA. While numerous myokines exhibited age-related differences, comprehensive cross-examination revealed that only four specific factors—CX3CL1, FGF21, IL-6, and Myostatin—exhibited protein concentrations in both serum and local muscle that were highly significantly correlated with MD levels (Figure 2D–G, Figure S3D–F). Consequently, these four molecules were designated as "key myokines" and utilized as reliable, high-fidelity biological proxies for the global skeletal muscle secretome in all subsequent analyses.

Beyond soluble proteins, we evaluated the extracellular vesicle (EV) secretory apparatus. Transcriptomic analyses revealed that EV-associated gene signatures correlated significantly and positively with MD scores, and were substantially enriched in the aged cohorts (Figure 2H, I, Figure S3G). To validate this functionally, EVs were strictly isolated from young and aged mice skeletal muscle via differential ultracentrifugation and characterized through morphological and quantitative profiling. Aged muscle released a significantly higher total concentration of EVs, displaying upregulated EV expression profiles compared to young tissues (Figure 2J–L, Figure S3H, I). Furthermore, immunohistochemical evaluation indicated a significant age-related elevation in RAB27A, a master regulator of vesicular docking and fusion (46). The protein levels of RAB27A, alongside established canonical EV tetraspanins CD9 and CD63 (47), exhibited strong positive correlations with the tissue MD burden (Figure 2J–L).

Localized Partial Reprogramming of Skeletal Muscle Attenuates MD, Accompanied by Secretome Rejuvenation, Rescued Bone Mass, and Partial Amelioration of Distant Senescence

Given the highly conserved correlation between MD and advancing age, coupled with the established capacity of partial epigenetic reprogramming to rejuvenate cellular identity, we hypothesized that targeted, localized partial reprogramming could reverse age-associated MD, rectify the dysregulated secretome, and subsequently rescue distant aging phenotypes, particularly in bone (48-50). We engineered a polycistronic AAV9 vector to drive the localized expression of mice Oct4, Sox2, and Klf4 (AAV-OSK), and administered it strictly via targeted localized intramuscular injection alongside an AAV-EGFP control. Mice were stratified into three experimental arms: Young + AAV-EGFP, Older + AAV-EGFP, and Older + AAV-OSK (Figure 3A).

We first confirmed the stringent spatial specificity and efficiency of our viral delivery system. Bulk RNA-seq and RT-qPCR of the skeletal muscle confirmed a robust upregulation of Oct4, Sox2, and Klf4 exclusively in the Older + AAV-OSK cohort (Figure 3B). Crucially, to ensure interventions were restricted to the local muscle microenvironment and circumvented systemic off-target effects, we evaluated OSK expression across major organs, including blood, bone matrix, bone marrow, liver, heart,

brain, spleen, kidney, and gut, detecting no significant ectopic expression (Figure S4A–C). Multiplex immunofluorescence (DAPI/EGFP/LAMININ/OCT4/KLF4) on muscle cross-sections further validated these findings. Due to the limited packaging capacity of the AAV genome, the AAV-OSK construct lacked an EGFP reporter; accordingly, while the AAV-EGFP cohorts displayed intense EGFP fluorescence with baseline endogenous OCT4/KLF4, the AAV-OSK cohort exhibited negligible EGFP but distinctly enriched focal expression of OCT4 and KLF4 (Figure 3C, D).

Targeted OSK delivery elicited profound local rejuvenation. Aged skeletal muscle was characterized by the striking accumulation of canonical senescence markers, specifically p16 and p21, a pathological burden that was significantly abrogated by localized AAV-OSK therapy (Figure 3E, F, Figure S4D). Concomitantly, the aging-induced surge in the MD transcriptomic signature was remarkably suppressed by the reprogramming intervention (Figure 3G). Furthermore, relative telomere length was demonstrably preserved in the OSK-treated muscle (Figure 3H). This molecular rejuvenation extended directly to the Senescence-Associated Secretory Phenotype (SASP) (Figure 3I, Figure S4E). Metabolically, the age-related impairment in mitochondrial oxygen consumption rate (OCR) was significantly rescued, denoting restored functional bioenergetics (Figure 3J).

Macroscopically, OSK intervention mitigated the severe muscle wasting characteristic of sarcopenia, significantly rescuing GA and QU absolute masses, specific muscle indices, and mean myofiber cross-sectional area (CSA) (Figure 3K, L). These morphometric improvements translated directly into functional rescue; the systemic exercise endurance (total exhaustion time and cumulative distance) and intrinsic specific tetanic torque, heavily compromised in aged mice, were robustly restored by OSK treatment (Figure 3M).

We subsequently evaluated the impact of local reprogramming on the skeletal muscle secretome. AAV-OSK potently repressed the globally elevated myokine signature and significantly reduced both the mRNA transcription and absolute protein concentrations of the four key circulating myokines (CX3CL1, FGF21, IL-6, and Myostatin) in aged muscle (Figure 3I, N, O, Figure S4F). Notably, the transcript levels of these factors remained unchanged in remote peripheral organs, confirming their muscle-specific origin (Figure S4G, H). Interestingly, despite static local mRNA expression in these distant tissues, the absolute protein levels of these myokines within those organs were significantly altered following muscle-targeted OSK therapy (Figure S5A). This dynamic perfectly reflects a canonical endocrine paradigm, establishing that the fluctuations of these factors in remote organs are explicitly driven by skeletal muscle-derived secretion. This was further evidenced by the significant modulation of these four myokines within the systemically circulating EV fractions (Figure S5B). Concurrently, the global transcriptomic signature of EV biogenesis was suppressed by OSK (Figure 4A). This was

functionally corroborated by a reduction in skeletal muscle RAB27A expression (via IHC) and a sharp decline in overall EV secretion concentrations, reversing the age-related vesicular hyperactivity (Figure 4B–D, Figure S5C, D).

Having established a fundamental remodeling of the muscle secretome, we sought to determine if this translated to phenotypic rescue in distal organs. We prioritized the skeletal system due to the tightly coupled, bi-directional muscle-bone endocrine axis. High-resolution micro-computed tomography (micro-CT) confirmed severe bone mineral density loss in aged mice; remarkably, strictly localized muscle reprogramming profoundly alleviated this osteoporotic decline (Figure 4E,F). This mitigation of bone loss was comprehensively validated by functional biomechanical testing, Masson's trichrome staining, and the quantification of specific structural markers (TRAP for osteoclasts; OCN and COL-1 for osteoblasts) (Figure 4G–I).

Finally, we performed a broad survey of systemic aging markers across distant organ systems, evaluating telomere length (Figure 4J), p16/p21 expression (Figure 4K, Figure S5E), SASP induction (Figure S6A), and mitochondrial respiration (Figure S6B). The magnitude of systemic rescue exhibited a degree of spatial heterogeneity. While the bone, which benefits from both systemic endocrine circulation and immediate localized paracrine cross-talk due to anatomical proximity, demonstrated remarkable recovery, other distant organs exhibited partial, though generally less pronounced, alleviation of senescence metrics. Together, these data orchestrate a novel physiological paradigm: localized partial reprogramming of aged skeletal muscle attenuates local mesenchymal drift, rehabilitates the multi-modal secretory profile, which phenotypically coincides with a robust rescue of age-related bone loss and a partial amelioration of distant organismal senescence.

Skeletal Muscle Partial Reprogramming Alleviates Bone Loss and Distant Senescence via Secretome Remodeling

To definitively establish a causal, mechanistic link between the OSK-rejuvenated skeletal muscle secretome and the observed downstream rescue of organ phenotypes, we employed a targeted "add-back" experimental paradigm. Following localized AAV-OSK partial reprogramming in 20-month-old mice, we attempted to artificially reconstruct the aged, hyper-secretory microenvironment, effectively aiming to neutralize the OSK-induced secretome rejuvenation (Figure 5A). To achieve this, OSK-treated mice were concurrently supplemented with either a defined recombinant "myokine mix" (comprising the four identified key myokines), purified extracellular vesicles (EVs) isolated from aged murine skeletal muscle, or a combination of both modalities. We first confirmed the fidelity of this delivery system; the administration of the myokine mix and the combination therapy significantly elevated the absolute protein concentrations of

these specific factors within both the local skeletal muscle tissue and the majority of distant target organs (Figure S7A).

We initially assessed the impact of this secretome reversal on the local skeletal muscle aging parameters. Notably, OSK treatment robustly restored local mitochondrial respiratory capacity and preserved relative telomere length (Figure 5B, C). The exogenous supplementation of the aged myokine mix, aged EVs, or their combination exerted no significant effect on these local intracellular metrics, a finding further validated by the persistent suppression of senescence markers p16 and p21 in the muscle tissue (Figure 5D–F). Furthermore, while total body weight remained statistically indistinguishable across all experimental cohorts (Figure 5G), the OSK-induced recovery of gross muscle mass and functional capacity was largely sustained. Although the add-back of the aged secretome components induced a slight trend toward impaired muscle mass and function, these effects did not reach statistical significance (Figure 5H–J). This critical dissociation implies that the primary local restorative effects of OSK partial reprogramming on myofiber integrity and local senescence are largely cell-autonomous, occurring independently of the bulk paracrine or endocrine secretome.

In stark contrast to the local muscle microenvironment, the downstream systemic benefits of localized OSK administration were fundamentally dependent on the rejuvenated secretory profile. While localized OSK significantly restored overall bone mineral density, the therapeutic add-back of the myokine mix, aged EVs, or the combination heavily blunted this osteogenic rescue, effectively reverting the bone density back toward the aged state (Figure 5K, L). This profound abrogation of bone recovery was further corroborated at the structural and material levels via comprehensive histological assessments and biomechanical testing (Figure 5M–O).

Finally, we expanded our evaluation to trace senescence markers across multiple distant target organs, including the skeletal system. Consistent with the macroscopic bone phenotypes, the forced re-introduction of the aged secretome components partially blunted the OSK-mediated systemic alleviation of aging. Specifically, in a subset of the evaluated organs, the supplementation of the myokine mix, EVs, or the combination prompted a moderate resurgence in p16 and p21 expression, alongside a measurable reduction in telomere length (Figure S7B). Together, these reversal experiments demonstrate that the profound remote osteo-protective benefits and the partial amelioration of senescence observed in specific distant tissues elicited by localized muscle reprogramming are causally mediated by the functional rejuvenation of the skeletal muscle secretome.

EGFR^{+} FAPs are the Principal Cellular Drivers of MD and the Skeletal Muscle Secretome

We next sought to resolve the precise cellular origins of mesenchymal drift (MD) and the skeletal muscle secretome. While the majority of existing research implicitly paradigms mature myofibers as the primary effectors of muscle-derived endocrine factors, we postulated that within the complex local microenvironment, non-myogenic resident populations might predominantly orchestrate these systemic functions. To investigate this hypothesis, we interrogated publicly available single-cell RNA-sequencing (scRNA-seq) datasets of human skeletal muscle from the GEO database. Applying stringent inclusion criteria, specifically requiring complete age-related clinical metadata and unsorted, whole-muscle single-cell profiling, we identified and incorporated two independent cohorts (41, 51): GSE167186 (6 young, 11 older subjects) and GSE268953 (5 young, 5 older subjects).

We projected the MD score, the curated myokine signature, and six distinct GO exosome signatures onto the identified cellular clusters. Strikingly, across all surveyed cell types, fibro-adipogenic progenitors (FAPs) exhibited the highest MD scores and myokine signatures in both independent datasets (Figure 6A–D). Furthermore, FAPs demonstrated robust enrichment for the exosomal signatures (Figure S8A, B). Crucially, when stratifying by age, the MD scores, myokine signatures, and exosome signatures within the FAP population were all significantly elevated in the aged cohorts compared to the young controls. This remarkable consistency strongly indicates that FAPs may serve as the pivotal cellular nexus linking age-related MD to the hyper-secretory phenotype.

Driven by this finding, we performed a high-resolution sub-clustering of the FAP population based on MD expression levels, delineating an MD-low subpopulation (FAP subtype 1) and an MD-high subpopulation (FAP subtype 2) (Figure 6E, F). Subsequent comparative analysis revealed that the age-driven exacerbations in both MD activity and myokine production were predominantly localized within FAP subtype 2 (FAP2). To decode the biological function of this specific subpopulation, we intersected the defining marker genes of FAP2 from both datasets and subjected the conserved gene set to GO pathway analysis. The FAP2 transcriptional network was overwhelmingly enriched for pathways governing "extracellular matrix organization" and "extracellular structure organization," seamlessly mirroring the core pathological features of MD (Figure 6G, Figure S8C). Consequently, FAP2 cells emerged as the definitive cellular source of the aberrant local secretory and MD profiles.

To establish a targetable molecular identity for this highly active FAP2 state, we intersected four distinct transcriptomic profiles: the FAP marker genes from both datasets, and the differentially expressed genes upregulated in aged versus young FAPs across both datasets. This multi-dimensional intersection yielded a single, highly conserved phenotypic marker: Epidermal Growth Factor Receptor (EGFR) (Figure 6H). EGFR was specifically and highly expressed in the FAP2 subpopulation, and its transcription was significantly upregulated in the aged cohorts (Figure 6I). Moreover, EGFR expression

exhibited a strong positive correlation with the MD score, myokine signature, and exosome biogenesis signatures at the single-cell level (Figure 6J, K).

To functionally validate this bioinformatic discovery in vivo, we transitioned back to our mice models, utilizing the established Young, Older, and Older + AAV-OSK cohorts. To preclude any potential fluorescence interference during fluorescence-activated cell sorting (FACS) from the AAV-EGFP reporter, we strictly utilized naive Young and Older mice as our baseline comparative controls. Conforming to established literature, total FAPs were defined and gated as Integrin $\alpha7^-$, $CD31^-$, $CD45^-$, and $Sca\text{-}1^+$. We subsequently isolated the target $EGFR^+$ FAP subpopulation via FACS (Figure S8D). Quantitative profiling revealed that the relative proportions of total FAPs to total cells, $EGFR^+$ FAPs to total cells, and specifically $EGFR^+$ FAPs within the total FAP pool, were all significantly increased in aged mice. Crucially, localized OSK partial reprogramming significantly reversed this pathological expansion, suppressing the $EGFR^+$ FAP population back toward youthful baselines (Figure 6L). This age-dependent expansion and its subsequent attenuation by OSK were definitively corroborated at the protein level via Western blotting for EGFR on the sorted FAP lysates (Figure 6M).

Activation of EGFR Drives the Secretory Phenotype in FAPs

To mechanistically dissect the function of EGFR in vitro, we stimulated primary FAPs with five widely validated recombinant EGFR ligands (Figure 7A). All five ligands promoted FAP fibrotic activation and elevated myokine mRNA expression to varying degrees (Figure S9A, B). At the functional level of protein and extracellular vesicle (EV) secretion, EGF and TGFA elicited the most potent induction of both myokine release and exosome secretion (Figure 7B, C). Interestingly, EGFR activation exerted no significant impact on the intrinsic cellular senescence phenotype of FAPs (Figure 7D, Figure S9B).

Given the superior activating efficacy of TGFA, we selected it as the primary ligand for subsequent downstream activation assays to evaluate the functional consequences of EGFR blockade (Figure 7E). Utilizing the selective EGFR inhibitor gefitinib, we observed that pharmacological blockade of EGFR significantly abolished TGFA-induced FAP fibrosis; however, consistent with our activation data, it failed to alter the senescence phenotype (Figure 7F–H). Crucially, EGFR inhibition potently restricted myokine expression and the concurrent release of myokines and EVs (Figure 7I, J, Figure S9C). To establish the cross-cellular relevance of this signaling axis, we co-cultured these pharmacologically treated FAPs with an established osteoblast cell line. TGFA stimulation of FAPs profoundly suppressed osteogenic gene expression in the co-cultured osteoblasts, a repression that was directly visualized and confirmed by markedly reduced Alkaline Phosphatase (ALP) and Alizarin Red S (ARS) staining (Figure 7K, L). Conversely, gefitinib treatment of FAPs effectively rescued the osteogenic capacity of the co-culture system. Collectively, these data establish EGFR as a pivotal regulatory

receptor dictating the FAP secretome and driving its subsequent pathological impact on osteoblasts.

We next explored the interplay between OSK-mediated partial reprogramming and the FAP secretome. We transduced primary FAPs with AAV-OSK to induce partial reprogramming, concurrently transfecting an EGFR overexpression (EGFR-OE) plasmid to uncouple EGFR signaling from the broader reprogramming network (Figure 7M). AAV-OSK effectively overexpressed the Oct4, Sox2, and Klf4 transgenes while simultaneously driving a significant reduction in endogenous Egfr expression (Figure S9D, E). The EGFR-OE construct successfully rescued this OSK-induced Egfr downregulation without interfering with the expression levels of the OSK reprogramming factors. Phenotypically, OSK reprogramming robustly suppressed FAP fibrosis, an effect that was actively neutralized by EGFR overexpression (Figure 7N, O, Figure S9F). Furthermore, AAV-OSK effectively preserved telomere length (Figure 7P), attenuated the p16 and p21 senescence phenotypes (Figure 7P, Figure S9F), enhanced mitochondrial respiration (Figure 7Q), and suppressed the Senescence-Associated Secretory Phenotype (SASP) (Figure 7R, Figure S9G). Notably, with the exception of its effect on the SASP, EGFR overexpression did not significantly alter any of the other fundamental senescence-associated phenotypes.

At the transcriptomic and secretory levels, AAV-OSK significantly reduced the MD score, the myokine signature, the expression of the four key myokines, the exosome biogenesis signature, and the absolute exosome concentration (Figure 7S–V, Figure S9H). The forced overexpression of EGFR effectively antagonized these secretory benefits, rescuing the hyper-secretory phenotype, although the specific reversion of the MD score did not reach strict statistical significance. This competitive dynamic was functionally validated in the osteoblast co-culture system, where EGFR overexpression effectively blunted the OSK-induced enhancement of osteogenic capacity (Figure 7W, X). Taken together, these findings suggest that EGFR acts primarily as a downstream effector of the aging program—intimately coupled to the SASP, myokine secretion, and exosome release—rather than a fundamental initiator of cellular senescence itself.

Targeted Lipid Nanoparticle Delivery of OSK and EGFR siRNA to FAPs Rejuvenates the Secretome, Rescues Bone Loss, and Partially Alleviates Distal Aging Phenotypes

Building upon our mechanistic delineation of the EGFR signaling axis, we sought to develop a therapeutically viable in vivo strategy to specifically target fibro-adipogenic progenitors (FAPs) for OSK-mediated partial reprogramming and targeted EGFR knockdown. Our goal was to engineer a precision intervention that maximizes positive systemic outcomes while minimizing potential off-target liabilities. To effectively package and deliver the large polycistronic OSK mRNA, we engineered targeted lipid

nanoparticles (LNPs) as our primary delivery vehicle (52, 53). We conjugated anti-PDGFRα antibodies to the LNP surface, leveraging PDGFRα as a highly specific and widely validated surface marker for FAPs (54, 55). By encapsulating either OSK mRNA or EGFR siRNA, we generated two targeted nano-formulations: Anti-PDGFRα-LNP@OSK and Anti-PDGFRα-LNP@EGFR-Si (Figure 8A).

Aged mice were stratified into five experimental cohorts: Control, Empty LNP, Anti-PDGFRα-LNP@OSK, Anti-PDGFRα-LNP@EGFR-Si, and a Combination group (co-administered with both active LNPs). Delivery validation confirmed that all three loaded LNP formulations achieved highly efficient and specific genetic editing strictly within the skeletal muscle FAP population (Figure 8B, Figure S10A–C). Crucially, no off-target payload accumulation or functional impact was detected in remote organs or non-FAP resident muscle cells, ensuring therapeutic specificity (Figure 8B, Figure S10A–C). Consequently, all three targeted treatments significantly attenuated mesenchymal drift (MD) levels locally within the skeletal muscle (Figure 8C).

We next evaluated the alleviation of intrinsic aging phenotypes. Consistent with our in vitro findings, both the LNP@OSK and combination therapies elicited a modest but significant preservation of telomere length (Figure 8D) and suppressed the expression of senescence markers p16 and p21 (Figure S10D, E). When evaluating the Senescence-Associated Secretory Phenotype (SASP), all three active interventions, LNP@OSK, LNP@EGFR-Si, and the combination, effectively blunted the local inflammatory profile (Figure 8E, Figure S10F). Furthermore, the profound rescue of mitochondrial respiratory capacity was exclusively driven by the OSK-containing formulations (LNP@OSK and combination), directly mirroring our prior cellular assays (Figure S10G). Macroscopically, however, all three targeted LNP groups successfully mitigated sarcopenic decline, yielding measurable improvements in both gross skeletal muscle mass and functional performance (Figure 8F, G, Figure S10H).

The local skeletal muscle secretory profile was robustly remodeled by these targeted interventions. All three therapeutic regimens significantly repressed the global myokine signature (Figure 8H) and drastically reduced both the mRNA expression and absolute protein secretion of the four key identified myokines (Figure 8I, J, Figure S10I). Systemically, while the intrinsic mRNA levels of these myokines in distant organs remained unaffected across the cohorts (Figure S10J–L), the absolute protein concentrations within those remote tissues exhibited significant alterations (Figure S11A–D). This pronounced transcript-protein decoupling directly highlights the canonical endocrine dynamic, confirming that skeletal muscle FAPs are the primary source of these systemic fluctuations. Parallel suppression was observed in the exosomal apparatus; the global exosome secretion signature (Figure S11E), the expression of the vesicular docking regulator RAB27A (Figure 8K, L), and the absolute concentration of released exosomes (Figure 8M) were significantly inhibited by all three LNP treatments.

Ultimately, this targeted attenuation of the FAP-driven hyper-secretory state translated into highly satisfactory therapeutic outcomes for distal bone metabolism. The targeted interventions effectively reversed age-related bone loss, a rescue comprehensively validated via structural histology (Figure 8N, O), functional biomechanical testing (Figure 8P, Figure S11F), and micro-CT morphometry (Figure 8Q, R). Beyond the skeletal system, the targeted ablation of the aging FAP secretome yielded heterogeneous but globally positive degrees of senescence alleviation across a broad spectrum of other distant target organs (Figure S11G, Figure S12). These data establish precision LNP-mediated targeting of FAPs as a highly translatable therapeutic avenue for mitigating systemic aging and rescuing osteoporotic decline.

Discussion

Aging is an intricately synchronized, multi-organ deterioration traditionally viewed through the lens of intrinsic cellular exhaustion and canonical senescence (56-58). Our findings establish a macro-systemic paradigm shift: the global progression of organismal aging may partly be orchestrated by localized structural and secretory alterations within peripheral tissues. We identify Mesenchymal Drift (MD) as a highly conserved transcriptomic and phenotypic hallmark of aged skeletal muscle, intimately coupled to functional decline, fibrosis, and sarcopenia.

Skeletal muscle is unequivocally recognized as a massive endocrine organ capable of exerting profound systemic effects via the secretion of circulating proteins, collectively termed myokines (59, 60). Under homeostatic conditions, these myokines mediate inter-organ cross-talk to regulate metabolic balance and tissue trophism (61, 62). However, we demonstrate that the chronological progression of MD corrupts this signaling network. The structural deterioration associated with MD fundamentally drives a hyper-secretory phenotype, characterized by the amplified release of pro-inflammatory factors and excessive extracellular vesicle (EV) biogenesis. This corrupted local microenvironment mimics the senescence-associated secretory phenotype (SASP), functionally converting skeletal muscle into a systemic engine of inflammaging that accelerates the degradation of remote organs.

A pivotal conceptual advance of this study lies in the experimental uncoupling of localized cellular senescence from systemic organismal decline. The canonical muscle-bone endocrine axis is well-documented, wherein age-related endocrine dysregulation severely compromises skeletal integrity and metabolism (63-65). Through in vivo partial reprogramming utilizing localized AAV-OSK delivery, we successfully attenuated local MD and suppressed the hyper-secretory phenotype, rescuing age-related osteoporotic bone loss.

Strikingly, our therapeutic "add-back" experiments revealed a strict biological dichotomy. While OSK reprogramming effectively restored intrinsic cellular parameters, such as myofiber mitochondrial bioenergetics and telomere length, independently of the surrounding secretome, the remote systemic benefits were entirely neutralized upon the exogenous reintroduction of the aged secretome. This definitively proves that while specific facets of tissue rejuvenation are purely cell-autonomous, the systemic mitigation of distal organ senescence relies partly on the functional, endocrine remodeling of the peripheral secretome.

Historically, mature multinucleated myofibers and $Pax7^+$ satellite cells have monopolized the focus of muscle-derived endocrine signaling (66-68). Here, we refine this anatomical resolution by identifying fibro-adipogenic progenitors (FAPs) as the principal cellular nodes driving MD and the aging secretome. FAPs are essential for maintaining muscle stem cell niches and coordinating regeneration; however, under pathological conditions or chronologic aging, they dictate fibro-fatty infiltration and subsequent muscle atrophy (60, 69, 70).

Through single-cell transcriptomics and flow cytometry, we mapped this maladaptive trajectory to an expanding, highly active $EGFR^+$ subpopulation of FAPs. Pharmacological blockade and genetic manipulation confirmed that EGFR signaling acts as a master regulator of FAP fibrotic activation and exosome release without fundamentally altering intrinsic senescence markers like p16 or p21. Thus, EGFR functions not as a passive biomarker of cellular aging, but as a critical effector node driving the pathological amplification of the local secretome.

Translating in vivo partial reprogramming into viable clinical therapies has been historically bottlenecked by the risks of teratoma formation, systemic toxicity, and off-target cellular dedifferentiation (71-73). By engineering anti-PDGFRα-guided lipid nanoparticles (LNPs), we achieved unprecedented spatial and cellular precision, delivering OSK mRNA and EGFR siRNA strictly to the resident FAP population. This targeted nanomedical intervention effectively circumvented systemic exposure while successfully reversing local MD, suppressing the pathological myokine and EV output, and robustly rescuing systemic bone loss.

While our study establishes MD and FAP-driven secretome remodeling as core drivers of aging, several limitations warrant future investigation. First, our in vivo "add-back" model utilized a defined cocktail of four key myokines alongside bulk EVs. The skeletal muscle secretome is inherently vast, and the exact stoichiometric interactions among uncharacterized circulating factors within the EV cargo remain to be fully mapped. Second, while we observed a profound morphometric and functional rescue in the skeletal system, the varied degrees of senescence alleviation in other remote organs suggest that tissue-specific receptor landscapes heavily dictate the penetrance of muscle-

derived endocrine signals. Finally, rigorous longitudinal studies in non-human primate models will be required to validate the long-term safety, durability, and multi-organ translatability of LNP-mediated epigenetic interventions.

Declaration of Interests

The authors declare no competing interests.

Fundings

This work was supported by Shanghai Pudong New Area Health Commission Young Scientific Project (PW2025B-24); Shanghai Pudong New Area Health Commission Outstanding Young Medical Talents Project (PWRq2025-02); Cell and Gene therapy project of the Shanghai Science and Technology Innovation action plan (23J11900400); Shanghai East Hospital characteristic professional subjects construction project (2024-DFTS-004).

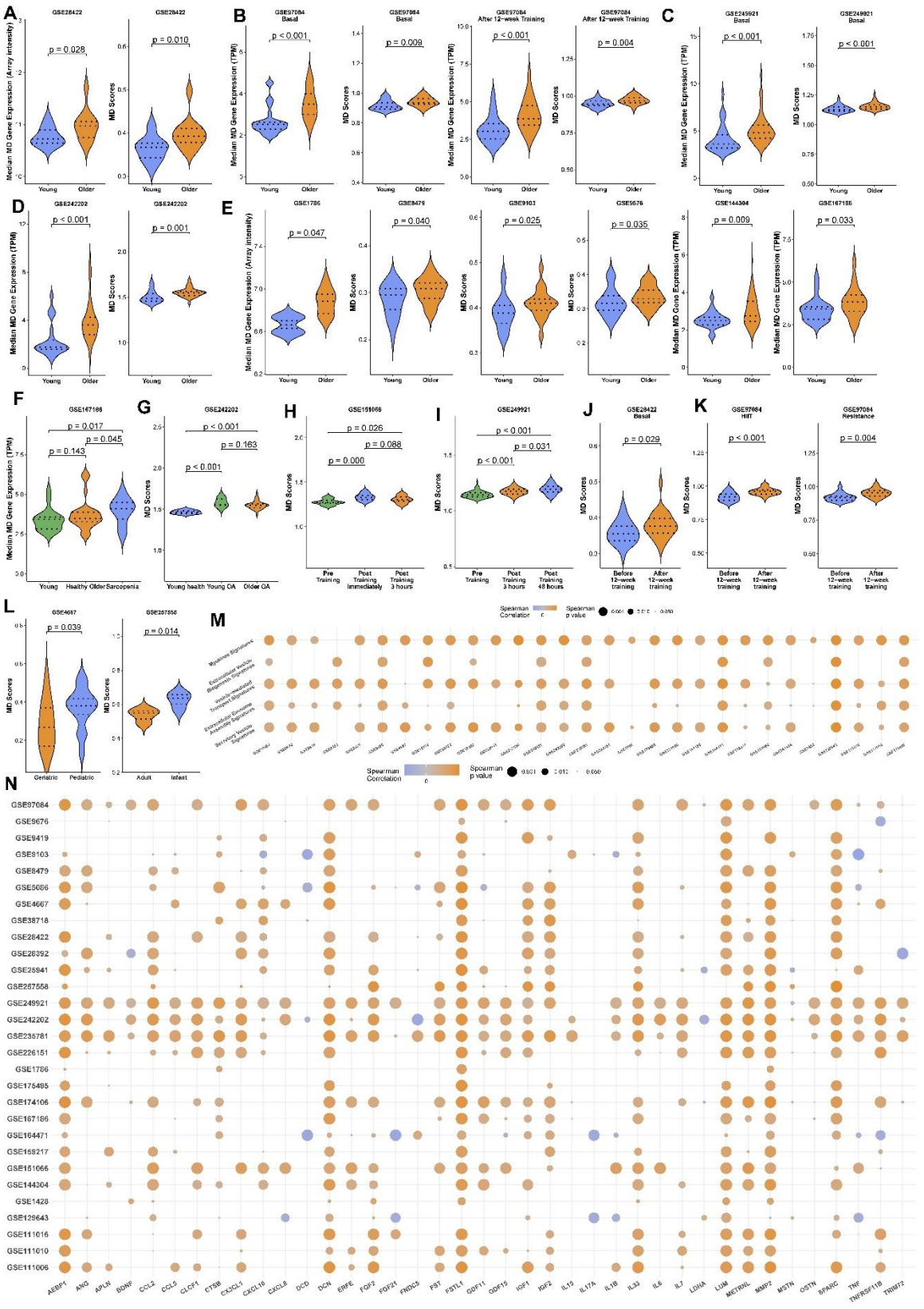

A
GSE28422
p = 0.028
GSE28422
p = 0.010
Median MD Gene Expression (Array intensity)
MD Scores
Young
Older
B
GSE97084 Basal
p < 0.001
GSE97084 Basal
p = 0.009
GSE97084 After 12−week Training
p < 0.001
GSE97084 After 12−week Training
p = 0.004
Median MD Gene Expression (TPM)
C
GSE249921 Basal
p < 0.001
GSE249921 Basal
p < 0.001
D
GSE242202
p < 0.001
GSE242202
p = 0.001
E
GSE1786
p = 0.047
GSE8479
p = 0.040
GSE9103
p = 0.025
GSE9676
p = 0.035
GSE144304
p = 0.009
GSE167186
p = 0.033
Median MD Gene Expression (Array intensity)
F
GSE167186
p = 0.017
p = 0.045
p = 0.143
Median MD Gene Expression (TPM)
Young
Healthy Older
Sarcopenia
G
GSE242202
p < 0.001
p = 0.163
p < 0.001
Young health
Young OA
Older OA
H
GSE151066
p = 0.026
p = 0.088
p = 0.000
Pre Training
Post Training immediately
Post Training 3 hours
I
GSE249921
p < 0.001
p = 0.031
p < 0.001
Pre Training
Post Training 3 hours
Post Training 48 hours
J
GSE28422 Basal
p = 0.029
Before 12−week training
After 12−week training
K
GSE97084 HIIT
p < 0.001
GSE97084 Resistance
p = 0.004
L
GSE4667
p = 0.039
GSE257558
p = 0.014
Geriatric
Pediatric
Adult
Infant
M
Spearman Correlation
Spearman p value
Myokines Signatures
Extracellular Matrix Biosynthesis Signatures
Vesicle-Mediated Transport Signatures
Extracellular Exosome Activities Signatures
Secreted Factors Signatures
N
GSE97084
GSE9676
GSE9419
GSE9103
GSE8479
GSE5086
GSE4667
GSE38718
GSE28422
GSE28392
GSE28941
GSE257558
GSE249921
GSE242202
GSE236781
GSE226151
GSE1786
GSE175495
GSE174106
GSE167186
GSE164471
GSE159217
GSE151066
GSE144304
GSE1428
GSE129643
GSE111016
GSE111010
GSE111006
AEBP1
ANG
APLN
BDNF
CCL2
CCL5
CLCF1
CTSB
CXCL1
CXCL16
CXCL8
DCD
DCN
EBFE
FGF2
FGF21
FNDC5
FST
FSTL1
GDF11
GDF15
IGF1
IGF2
IL15
IL17A
IL1B
IL33
IL6
IL7
LDHA
LUM
METRNL
MMP2
MSTN
OSTN
SPARC
TNF
TNFRSF11B
TRIM72

Figure 1. MD in Skeletal Muscle is a Prevalent Hallmark of Aging and Muscle Status and related to Skeletal Muscle Secretome in Humans. (A) MD levels in young and older individuals from the GSE28422 cohort. (B) MD levels before and after a 12-week training intervention in the GSE97084 cohort. (C) Baseline MD levels in young and older cohorts prior to acute exercise in the GSE249921 dataset. (D) MD levels in young and older individuals from the GSE242202 cohort. (E) MD levels in young and older individuals across a multitude of additional independent human datasets. (F) MD levels in healthy young, healthy older, and older individuals diagnosed with sarcopenia from the GSE167186 dataset. (G) MD levels in healthy young, young with osteoarthritis (OA), and older adults with OA in the GSE242202 dataset. (H and I) Dynamic fluctuations of MD levels in response to an acute exercise in the GSE151066dataset (H) and GSE249921 dataset (I). (J and K) Long-term adaptations of the MD signature following 12 weeks of training in the GSE28422 (J) and GSE97084 datasets (K). (L) Evaluation of MD levels including pediatric skeletal muscle in the GSE4667 and GSE257558 dataset. (M) Spearman rank correlations mapping MD scores against Myokines signatures, Extracellular Vesicle Biogenesis, Vesicle-mediated Transport, Extracellular Exosome Assembly, and Secretory Vesicle across diverse human cohorts. (N) Spearman rank correlations mapping MD scores against individual transcript profiles of myokine genes. Transcript abundances were measured as transcripts per million (TPM) in RNA-seq cohorts and normalized signal intensities for microarray datasets. Bivariate correlation analyses were systematically performed using non-parametric Spearman's rank correlation. Two-group and multi-group comparisons were evaluated utilizing independent Student's t-tests, Wilcoxon rank-sum tests, one-way ANOVA followed by Tukey's post hoc test, or the Kruskal-Wallis test followed by Dunn's multiple comparisons test, dependent upon data normality. Exact p values are indicated within the panels. See also Figures S1 and S2.

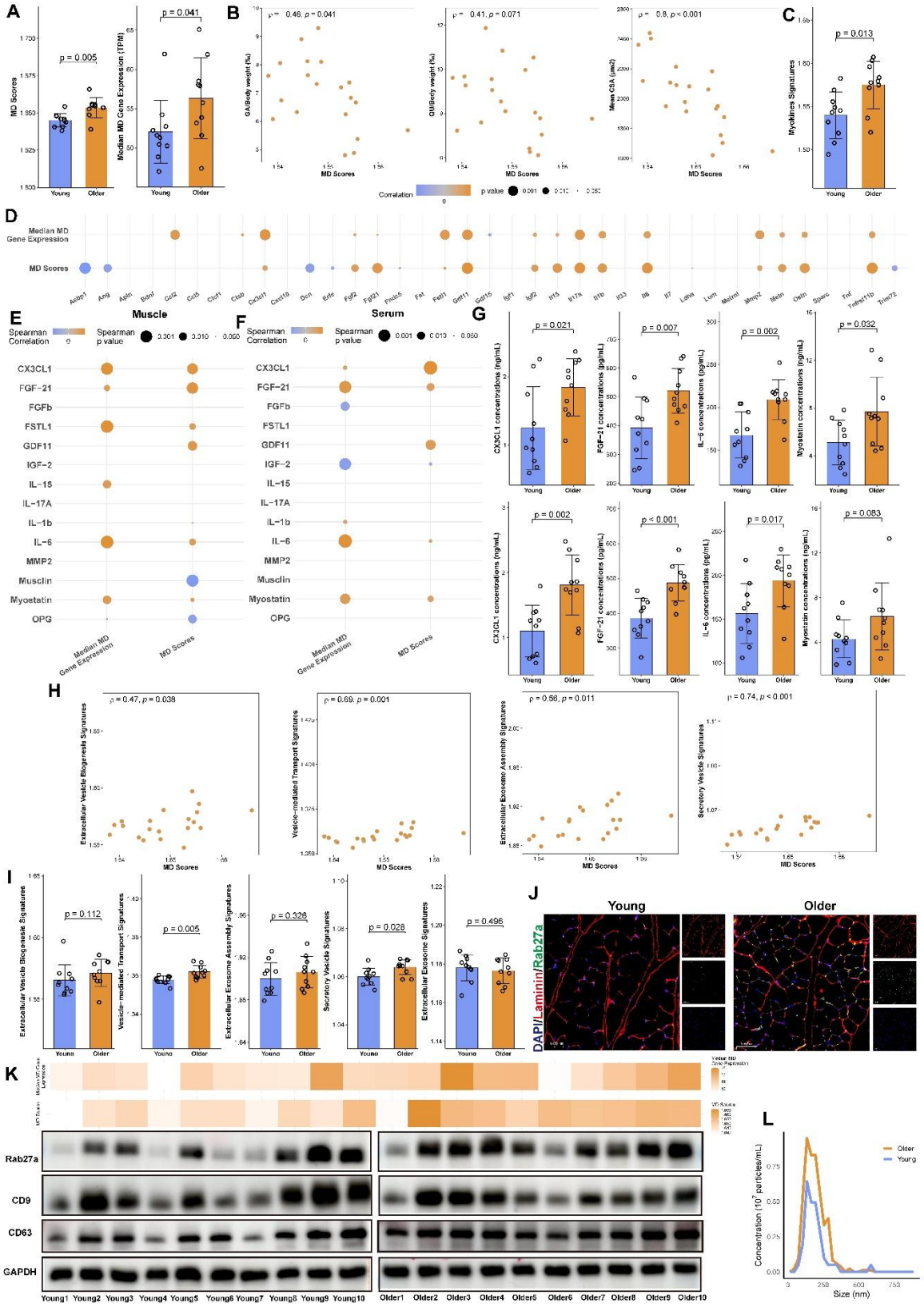

A
MD Scores
p = 0.005
Young
Older
Median MD Gene Expression (TPM)
p = 0.041
B
ρ = 0.46, p = 0.041
GA/Body weight (%)
MD Scores
ρ = 0.41, p = 0.071
QU/Body weight (%)
ρ = 0.8, p < 0.001
Mean CSA (μm2)
Correlation
p value
C
Myokines Signatures
p = 0.013
D
Median MD Gene Expression
MD Scores
Acbp1 Arg Apln Bdnf Cst2 Cst5 Ctnf1 Ctsb Cxcl1 Cxcl10 Dcn Ereg Fgf2 Fgf21 Fndc5 Fst Fstl1 Gdf11 Gdf15 Igf1 Igf2 Il15 Il17a Il1b Il33 Il6 Il7 Lcn2 Lum Metrnl Mmp2 Mstn Oxtn Sparc Tnf Tnfrsf11b Tnfrsf21
E
Muscle
Spearman Correlation
Spearman p value
CX3CL1 FGF-21 FGFb FSTL1 GDF11 IGF-2 IL-15 IL-17A IL-1b IL-6 MMP2 Musclin Myostatin OPG
Median MD Gene Expression
MD Scores
F
Serum
G
CX3CL1 concentrations (ng/mL)
p = 0.021
FGF-21 concentrations (pg/mL)
p = 0.007
IL-6 concentrations (pg/mL)
p = 0.002
Myostatin concentrations (ng/mL)
p = 0.032
p = 0.002
p < 0.001
p = 0.017
p = 0.083
H
Extracellular Vesicle Biogenesis Signatures
ρ = 0.47, p = 0.038
Vesicle-mediated Transport Signatures
ρ = 0.69, p = 0.001
Extracellular Exosome Assembly Signatures
ρ = 0.56, p = 0.011
Secretory Vesicle Signatures
ρ = 0.74, p < 0.001
MD Scores
I
p = 0.112
p = 0.005
p = 0.326
p = 0.028
p = 0.496
J
Young
Older
DAPI/Laminin/Rab27a
K
Rab27a
CD9
CD63
GAPDH
Young1 Young2 Young3 Young4 Young5 Young6 Young7 Young8 Young9 Young10
Older1 Older2 Older3 Older4 Older5 Older6 Older7 Older8 Older9 Older10
L
Concentration (10^7 particles/mL)
Size (nm)
Older
Young

Figure 2. Age-Dependent MD and the Skeletal Muscle Secretome Profile in Mice Models. (A) MD levels in aged (20-month-old) versus young (4-month-old) mice skeletal muscle. (B) Correlation mapping demonstrating robust negative associations between global MD levels and core morphometric indices of muscle mass: gastrocnemius (GA) /body weight, quadriceps (QU) /body weight, and mean CSA. (C) Comparison of the myokine signature between young and aged mice skeletal muscle. (D) Spearman correlation heatmaps detailing the transcriptional dependencies between global MD levels (MD scores and median MD gene expression) and the mRNA expression of myokines. (E and F) Spearman correlation heatmaps detailing the transcriptional dependencies between global MD levels and the protein concentrations of multiple specific myokines in muscle (E) and serum (F). (G) Protein concentrations of CX3CL1, FGF21, IL-6, and Myostatin within skeletal muscle and serum. (H) Spearman correlation between MD scores and EV-related signatures. (I) Comparison of the EV-related signatures between young and aged mice skeletal muscle. (J) Representative multiplex immunofluorescence staining (DAPI/LAMININ/RAB27A) mapping the spatial localization and age-related enrichment of RAB27A within the skeletal muscle microenvironment. (K) Western blot analysis (RAB27A, CD9, CD63) and corresponding MD levels. (L) Nanoparticle Tracking Analysis (NTA) determining the absolute concentration and particle size distribution of strictly isolated EVs from young and aged mice skeletal muscle. In vivo models utilized n = 10 biologically independent animals per age cohort. Bivariate statistical dependencies were ascertained utilizing non-parametric Spearman's rank correlation analysis. Comparisons between young and older groups were evaluated using independent Student's t-tests or Wilcoxon rank-sum tests, dependent upon the normality of data distribution. Exact p values and Spearman r values are displayed within the respective panels.

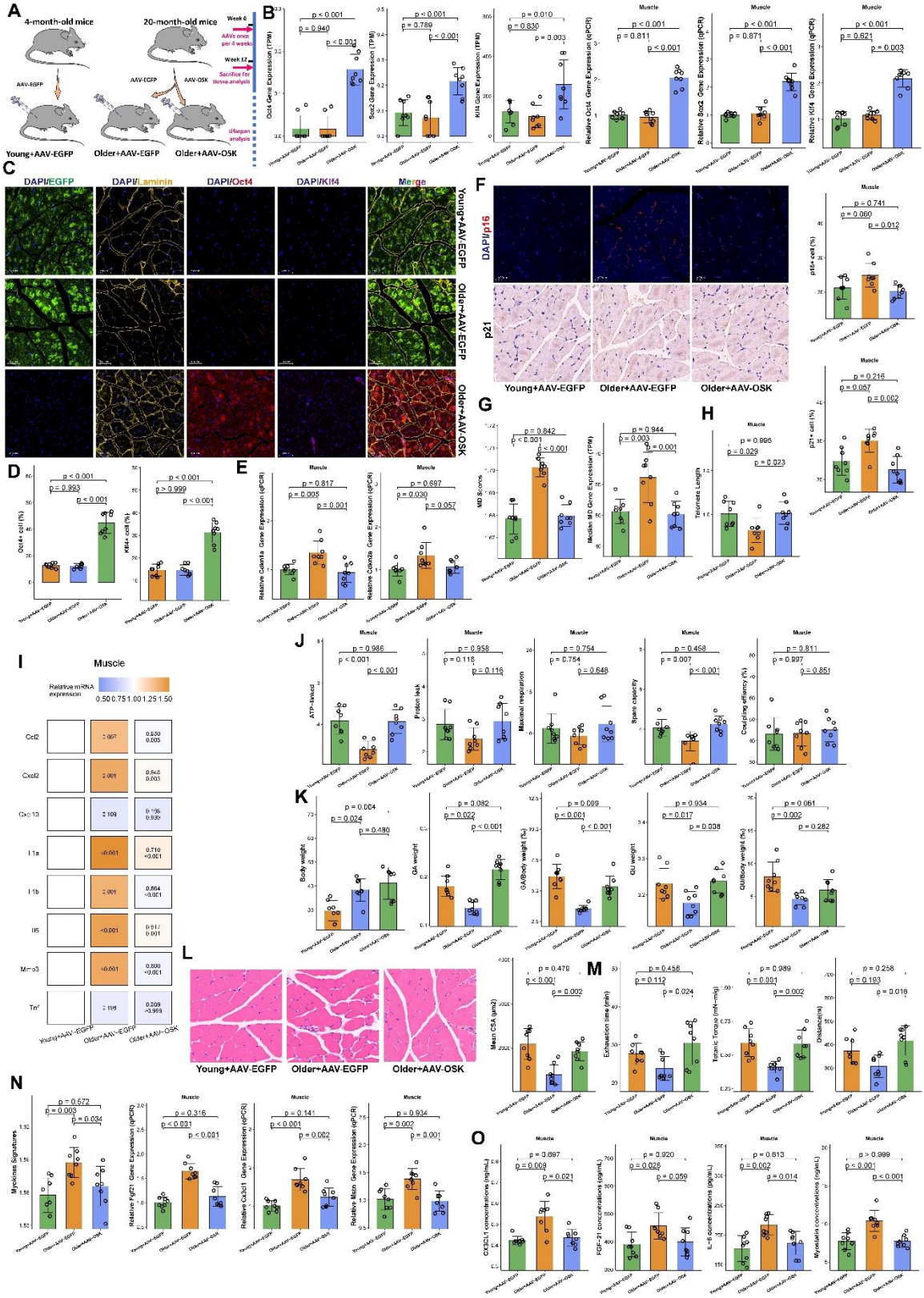

A
4-month-old mice
20-month-old mice
Week 0
AAVs once per 4 weeks
Week 12
Sacrifice for tissue analysis
AAV-EGFP
AAV-OSK
Lifespan analysis
Young+AAV-EGFP
Older+AAV-EGFP
Older+AAV-OSK
B
Oct4 Gene Expression (TPM)
Sox2 Gene Expression (TPM)
Klf4 Gene Expression (TPM)
Relative Oct4 Gene Expression (qPCR)
Relative Sox2 Gene Expression (qPCR)
Relative Klf4 Gene Expression (qPCR)
Muscle
C
DAPI/EGFP
DAPI/Laminin
DAPI/Oct4
DAPI/Klf4
Merge
Young+AAV-EGFP
Older+AAV-EGFP
Older+AAV-OSK
D
Oct4+ cell (%)
Klf4+ cell (%)
E
Relative Cdkn1a Gene Expression (qPCR)
Relative Cdkn2a Gene Expression (qPCR)
Muscle
F
DAPI/p16
p21
p16+ cell (%)
p21+ cell (%)
Young+AAV-EGFP
Older+AAV-EGFP
Older+AAV-OSK
G
MD Scores
Median MD Gene Expression (TPM)
H
Telomere Length
Muscle
I
Muscle
Relative mRNA expression
0.50 0.75 1.00 1.25 1.50
Ccl2
Cxcl2
Cxcl10
Il1a
Il1b
Il6
Mmp3
Tnf
Young+AAV-EGFP
Older+AAV-EGFP
Older+AAV-OSK
J
ATP-linked
Proton leak
Maximal respiration
Spare capacity
Coupling efficiency (%)
Muscle
K
Body weight
GA weight
GA/Body weight (%)
QU weight
QU/Body weight (%)
L
Young+AAV-EGFP
Older+AAV-EGFP
Older+AAV-OSK
M
Mean CSA (μm2)
Extraction time (min)
Tetanic Torque (mN·m/g)
Distance(m)
N
Myokines Signatures
Relative Fgf21 Gene Expression (qPCR)
Relative Cxcl1 Gene Expression (qPCR)
Relative Mstn Gene Expression (qPCR)
Muscle
O
CXCL1 concentrations (ng/mL)
FGF-21 concentrations (pg/mL)
IL-6 concentrations (pg/mL)
Myostatin concentrations (ng/mL)
Muscle

Figure 3. Localized partial reprogramming of skeletal muscle attenuates MD, accompanied by secretome rejuvenation, rescued muscle mass, and functional recovery. (A) Schematic representation of the experimental paradigm for targeted localized intramuscular administration of AAV-OSK and AAV-EGFP in 20-month-old mice. (B) RNA-seq and RT-qPCR validation of localized Oct4, Sox2, and Klf4 transcript upregulation exclusively within the AAV-OSK treated skeletal muscle. (C and D) Representative multiplex immunofluorescence images of DAPI, EGFP, LAMININ, OCT4, and KLF4 (C) and corresponding quantifications (D). (E and F) Evaluation of local cellular senescence via relative mRNA expression of Cdkn1a (p21) and Cdkn2a (p16) (E), alongside representative immunofluorescence staining and quantifications for p16 and p21 (F). (G) Reversal of MD, quantified via GSEA-derived MD scores and median MD gene expression. (H) Preservation of relative telomere length in OSK-treated skeletal muscle, quantified independently via qPCR. (I) Transcriptional suppression of the Senescence-Associated Secretory Phenotype (SASP) components (Ccl2, Cxcl2, Cxcl10, Il1a, Il1b, Il6, Mmp3, Tnf) within the local microenvironment. (J) Mitochondrial oxygen consumption rate (OCR), systematically evaluating core bioenergetic parameters including ATP-linked respiration, proton leak, maximal respiration, spare capacity, and coupling efficiency (%), demonstrating significantly restored functional bioenergetics. (K and L) Macroscopic morphometric (K), and representative H&E staining with mean myofiber cross-sectional area (CSA) quantification (L). (M) Functional rescue of systemic exercise endurance (total exhaustion time and cumulative distance) and intrinsic specific tetanic torque. (N and O) Potent repression of the global myokine signature and key myokines (N) and absolute protein concentrations (O) of the four key circulating myokines (CX3CL1, FGF21, IL-6, and Myostatin) within the local muscle tissue. n = 8 biologically independent animals per cohort. Data are represented as mean ± SD. Statistical significance was determined utilizing one-way ANOVA followed by Tukey's post hoc test or the Kruskal-Wallis test followed by Dunn's multiple comparisons test. Exact p values are indicated within the respective panels.

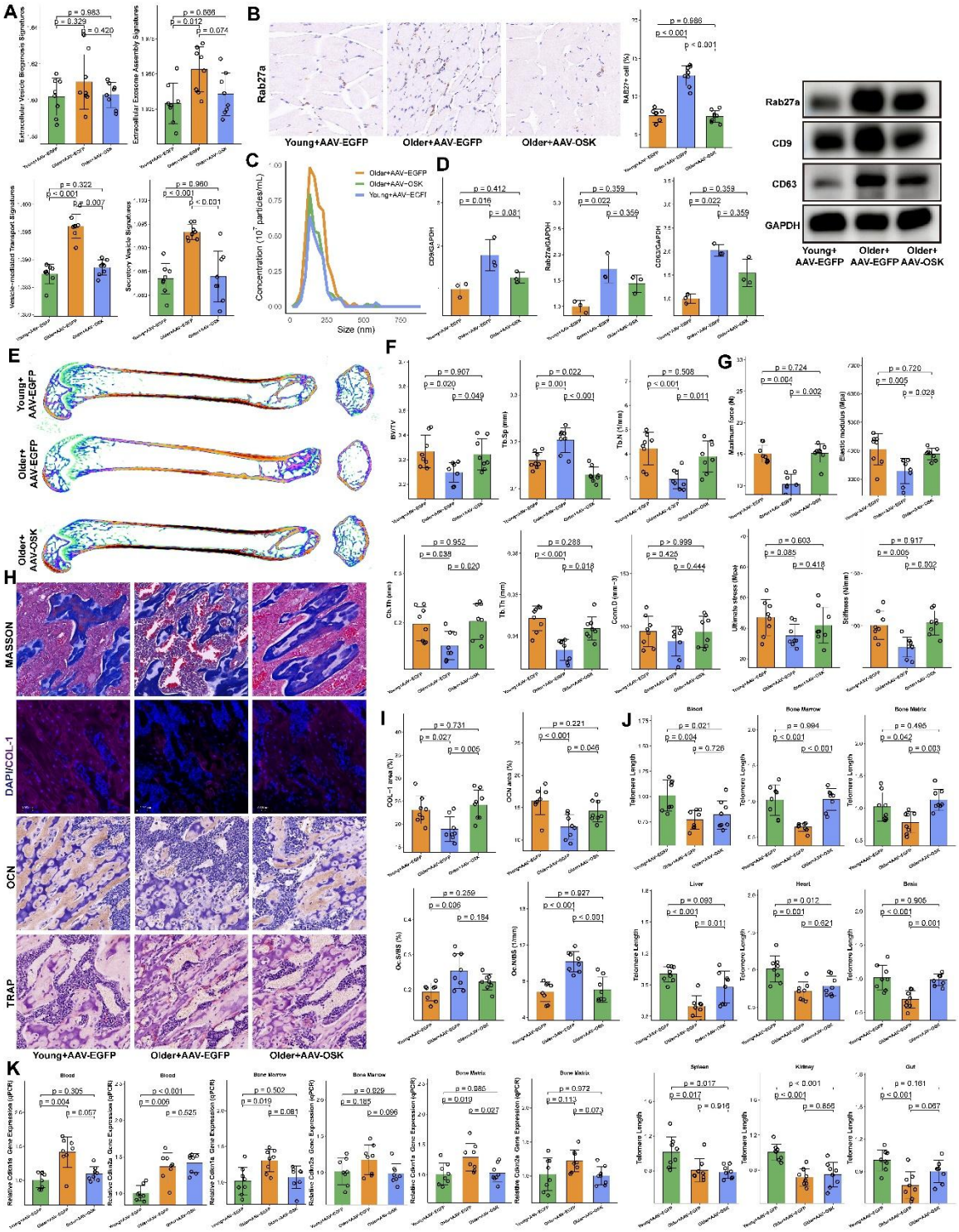


Figure 4. Skeletal muscle partial reprogramming alleviates bone loss and partially ameliorates distant senescence via secretome remodeling. (A) Suppression of the global transcriptomic signature of EVs following localized OSK intervention. (B)

Representative IHC staining and quantifications of RAB27A. (C) EV secretion concentrations and particle size distributions. (D) Western blot evaluation of RAB27A and canonical EV tetraspanins (CD9, CD63). (E and F) Representative Micro-CT reconstructions (E) and quantifications (F) of the harvested mice femurs. (G) Biomechanical 3-point bending test parameters. (H and I) Representative images (H) of Masson's staining, immunostaining of COL-1 and OCN, and TRAP staining and subsequent quantifications (I). (J) telomere length across multiple organs. (K) Cdkn2a (p16) and Cdkn1a (p21) expression in blood, bone marrow, and bone matrix. n = 8 biologically independent animals per cohort. Data are represented as mean ± SD. Statistical significance was determined utilizing one-way ANOVA followed by Tukey's post hoc test or the Kruskal-Wallis test followed by Dunn's multiple comparisons test. Exact p values are indicated within the respective panels.

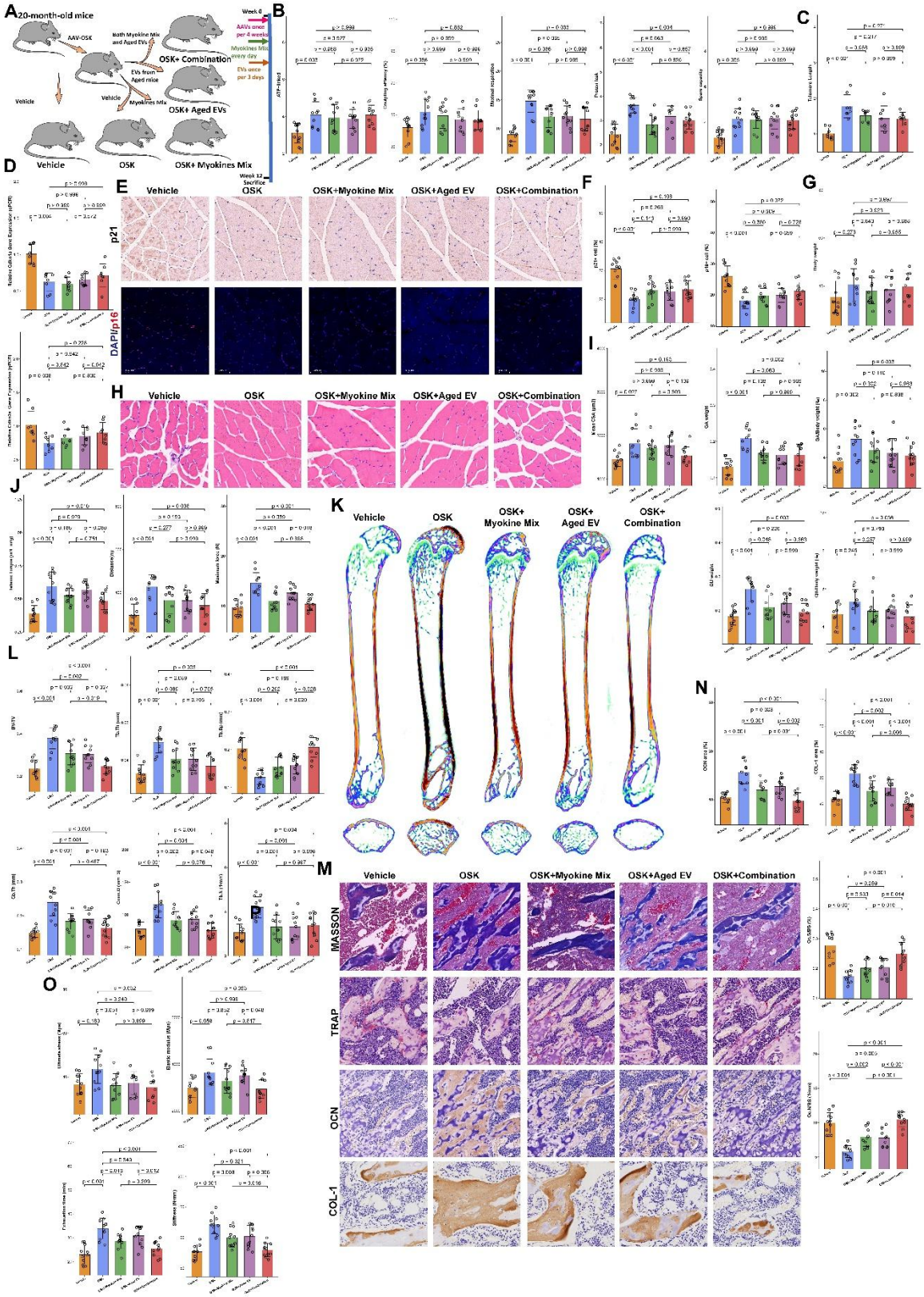

A
20-month-old mice
AAV-OSK
Both Myokine Mix and Aged EVs
OSK+ Combination
EVs from Aged mice
Vehicle
Myokines Mix
OSK+ Aged EVs
Vehicle
OSK
OSK+ Myokines Mix
Week 0
AAVs once per 4 weeks
Myokines Mix every day
EVs once per 3 days
Week 12 Sacrifice
B
C
D
E
Vehicle
OSK
OSK+Myokine Mix
OSK+Aged EV
OSK+Combination
p21
DAPI/p16
F
G
H
Vehicle
OSK
OSK+Myokine Mix
OSK+Aged EV
OSK+Combination
I
J
K
Vehicle
OSK
OSK+ Myokine Mix
OSK+ Aged EV
OSK+ Combination
L
M
Vehicle
OSK
OSK+Myokine Mix
OSK+Aged EV
OSK+Combination
MASSON
TRAP
OCN
COL-1
N
O

Figure 5. Partial reprogramming alleviates bone loss and distant senescence via secretome remodeling. (A) Schematic overview of the experimental paradigm. (B) Skeletal muscle mitochondrial respiratory capacity (ATP-linked respiration, coupling efficiency, maximal respiration, proton leak, and spare capacity) across groups. (C) Relative telomere length across groups. (D-F) Evaluation of local cellular senescence via relative mRNA expression of Cdkn1a (p21) and Cdkn2a (p16) (D), alongside representative immunofluorescence staining (E) and quantifications (F) for p16 and p21. (G-I) Body weight (G), representative H&E staining (H) with mean myofiber cross-sectional area (CSA) quantification (I), and macroscopic morphometric (I). (J) Functional rescue of systemic exercise endurance (total exhaustion time and cumulative distance) and intrinsic specific tetanic torque. (K and L) Representative Micro-CT reconstructions (K) and quantifications (L) of the harvested mice femurs. (M and N) Representative images (M) of Masson's staining, immunostaining of COL-1 and OCN, and TRAP staining and subsequent quantifications (N). (O) Biomechanical 3-point bending test parameters. n = 11 biologically independent animals per cohort. Data are represented as mean ± SD. Statistical significance was determined utilizing one-way ANOVA followed by Tukey's post hoc test or the Kruskal-Wallis test followed by Dunn's multiple comparisons test. Exact p values are indicated within the respective panels.

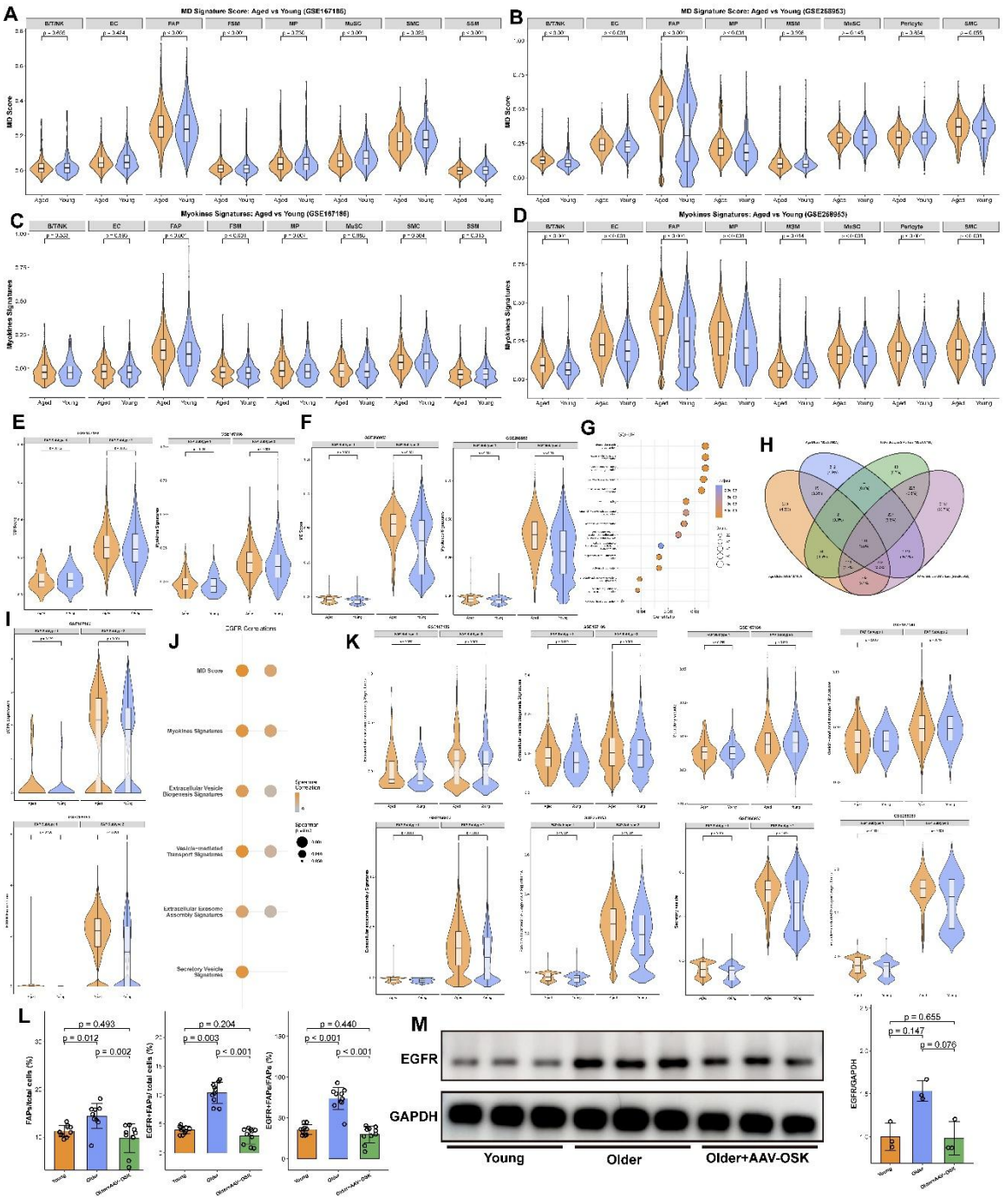


Figure 6. EGFR⁺ FAPs are the Principal Cellular Drivers of MD and the Skeletal Muscle Secretome. (A and B) MD scores in aged and young populations across all identified cell types in GSE167186 (A) and GSE268953 (B) datasets. (C and D) myokines signatures in aged and young populations across all identified cell types in GSE167186 (C) and GSE268953 (D) datasets. (E and F) MD scores and myokines signatures in aged and young populations across FAPs subtypes in GSE167186 (E) and GSE268953 (F) datasets. (G) Gene Ontology (GO) functional enrichment analysis of

FAPs subtype 2 marker genes. (H) The intersection of marker genes of FAPs subtype 2 marker genes from two datasets. (I) EGFR expression in aged and young populations across FAPs subtypes in GSE167186 and GSE268953 datasets. (J) Spearman rank correlations mapping EGFR expression against Myokines signatures, Extracellular Vesicle Biogenesis, Vesicle-mediated Transport, Extracellular Exosome Assembly, and Secretory Vesicle across all cells in GSE167186 and GSE268953 datasets. (K) EV-related signatures in aged and young populations across FAPs subtypes in GSE167186 and GSE268953 datasets. (L) In vivo validation via fluorescence-activated cell sorting (FACS). (M) Western blot validation of EGFR protein levels on the sorted FAPs. n = 10 biologically independent animals per cohort. Bivariate correlation analyses were executed utilizing non-parametric Spearman's rank correlation. Comparisons among groups were evaluated utilizing one-way ANOVA followed by Tukey's post hoc test or the Kruskal-Wallis test followed by Dunn's multiple comparisons test.

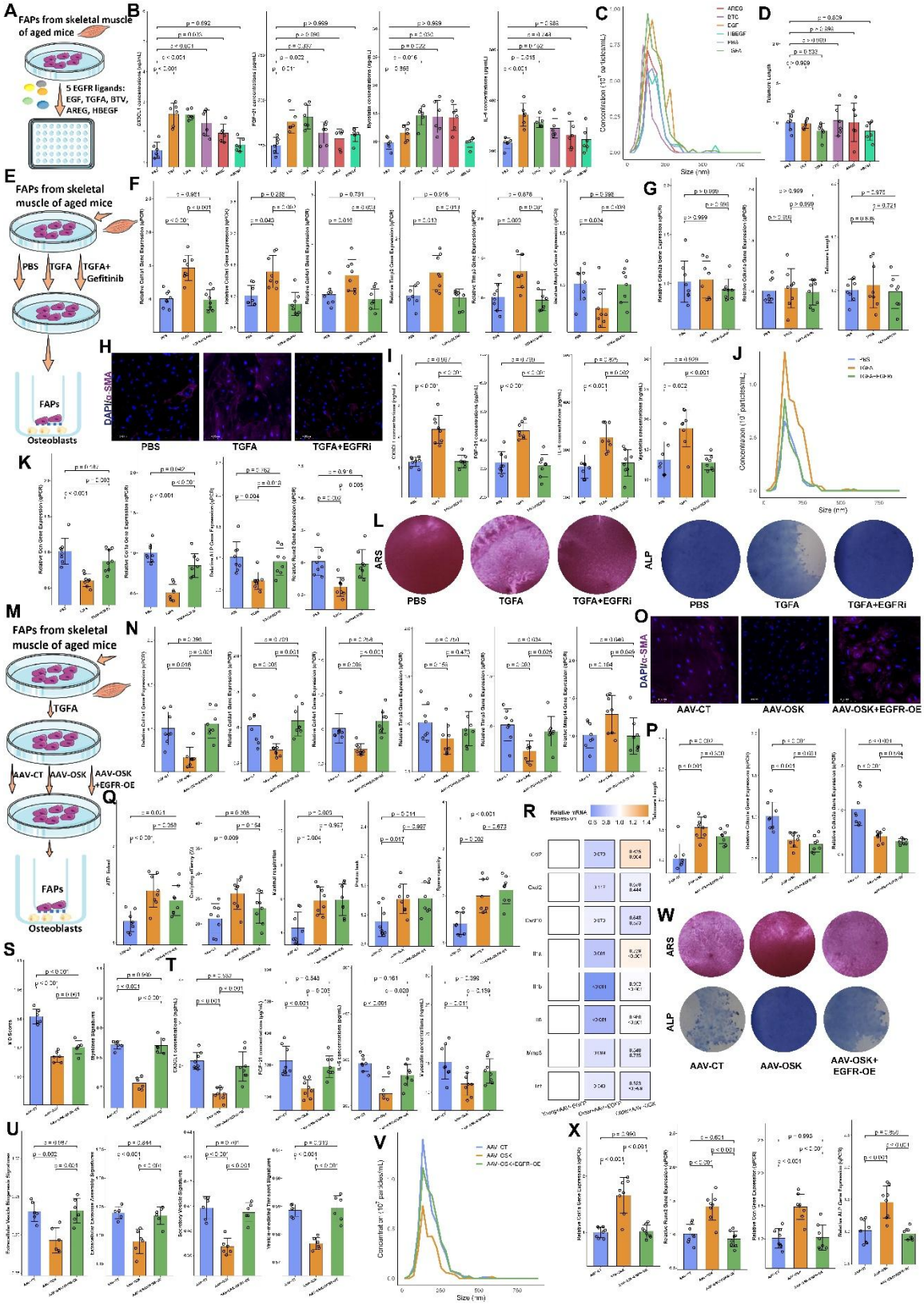

A
FAPs from skeletal muscle of aged mice
5 EGFR ligands: EGF, TGFA, BTV, AREG, HBEGF
B
C
D
E
FAPs from skeletal muscle of aged mice
PBS
TGFA
TGFA+ Gefitinib
FAPs
Osteoblasts
F
G
H
DAPI/α-SMA
PBS
TGFA
TGFA+EGFRi
I
J
K
L
ARS
ALP
PBS
TGFA
TGFA+EGFRi
M
FAPs from skeletal muscle of aged mice
TGFA
AAV-CT
AAV-OSK
AAV-OSK +EGFR-OE
FAPs
Osteoblasts
N
O
DAPI/α-SMA
AAV-CT
AAV-OSK
AAV-OSK+EGFR-OE
P
Q
R
S
T
U
V
Concentration (10^7 particles/mL)
Size (nm)
AAV-CT
AAV-OSK
AAV-OSK+EGFR-OE
W
ARS
ALP
AAV-CT
AAV-OSK
AAV-OSK+ EGFR-OE
X

Figure 7. Activation of EGFR Drives the Secretory Phenotype in FAPs. (A) In vitro functional activation of primary FAPs utilizing five recombinant EGFR ligands (EGF, TGFA, BTC, AREG, and HBEGF). (B) Protein concentrations of the four key circulating myokines (CX3CL1, FGF21, IL-6, and Myostatin). (C) EV secretion concentrations and particle size distributions. (D) telomere length across FAPs activated by different ligands. (E) Pharmacological blockade of EGFR signaling. (F) Fibrosis gene expression of FAPs. (G) Cdkn2a (p16) and Cdkn1a (p21) expression and telomere length of FAPs. (H) Representative immunofluorescence staining of α-SMA. (I) Protein concentrations of the four key circulating myokines. (J) EV secretion concentrations and particle size distributions. (K) Osteogenesis gene expression of osteoblasts co-cultured with FAPs. (L) ARS and ALP staining of osteoblasts co-cultured with FAPs. (M) Experimental design illustrating primary FAPs transduced with AAV-OSK to induce partial reprogramming, concurrently transfected with an EGFR overexpression (EGFR-OE) plasmid to uncouple EGFR signaling. (N) Fibrosis gene expression of FAPs. (O) Representative immunofluorescence staining of α-SMA. (P) Cdkn2a (p16) and Cdkn1a (p21) expression and telomere length of FAPs. (Q) Mitochondrial respiratory capacity of FAPs. (R) mRNA levels of SASP components. (S) MD scores and myokines signatures. (T) Protein concentrations of the four key circulating myokines. (U) EV-related signatures. (V) EV secretion concentrations and particle size distributions. (W) ARS and ALP staining of osteoblasts co-cultured with FAPs. (X) Osteogenesis gene expression of osteoblasts co-cultured with FAPs. n = 6 or 8 per group. Bivariate correlation analyses were executed utilizing non-parametric Spearman's rank correlation. Comparisons among groups were evaluated utilizing one-way ANOVA followed by Tukey's post hoc test or the Kruskal-Wallis test followed by Dunn's multiple comparisons test.

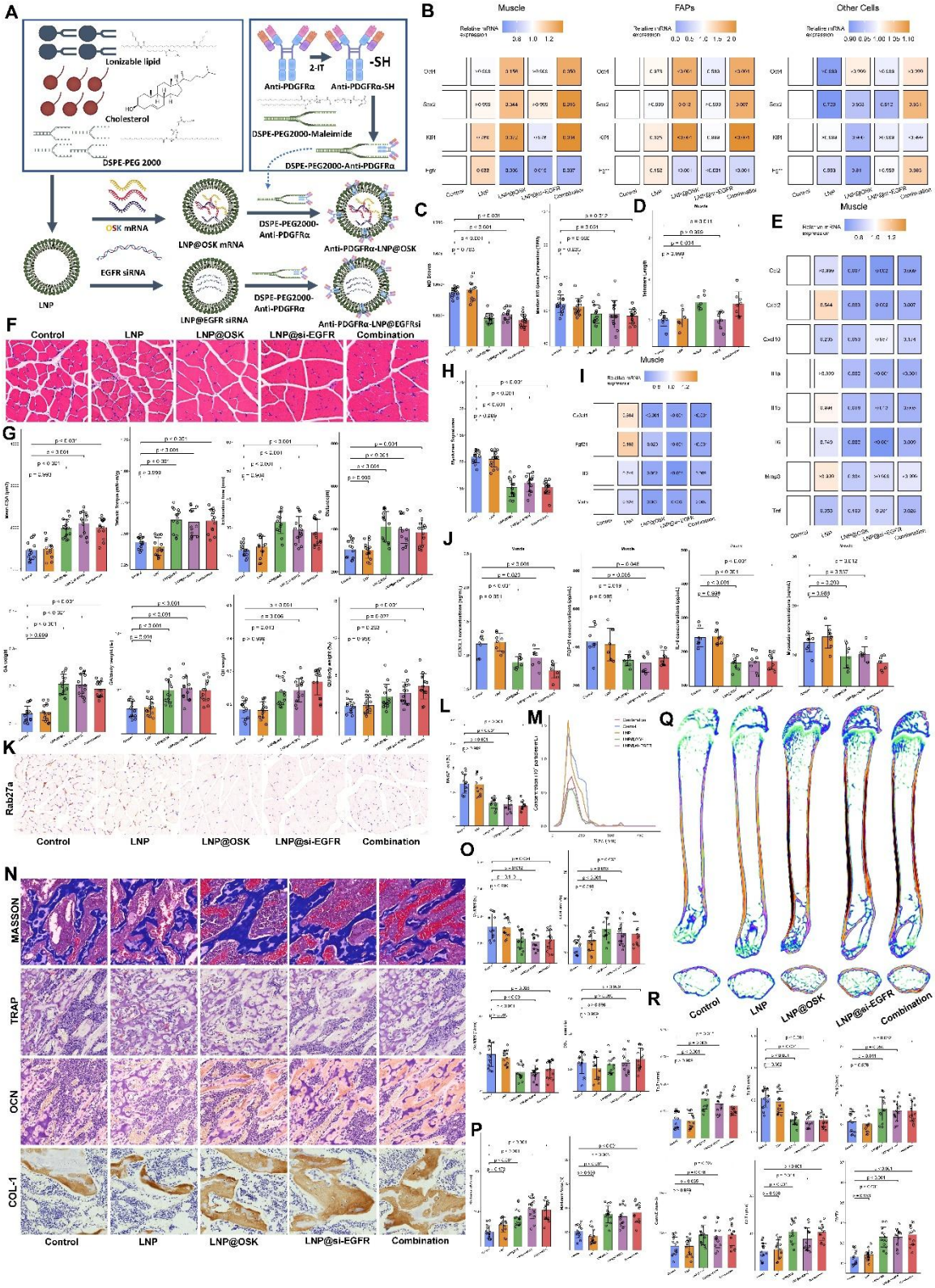


Figure 8. Targeted Lipid Nanoparticle Delivery of OSK and EGFR siRNA to FAPs Rejuvenates the Secretome, Rescues Bone Loss, and Alleviates Distal Aging

Phenotypes. (A) Schematic representation of precision therapeutic engineering. Targeted lipid nanoparticles (LNPs) conjugated with anti-PDGFRα antibodies encapsulating either OSK mRNA (Anti-PDGFRα-LNP@OSK) or EGFR siRNA (Anti-PDGFRα-LNP@EGFR-Si). (B) RT-qPCR validation of Egfr, Oct4, Sox2, and Klf4 transcript confirming highly efficient and specific genetic editing strictly within the targeted skeletal muscle FAP population. (C) MD levels in skeletal muscle with different targeted LNP interventions. (D) Telomere length across different groups. (E) mRNA levels of SASP components. (F and G) Representative H&E staining (F) with mean myofiber cross-sectional area (CSA) quantification, exercise functions and macroscopic morphometric (G). (H) Myokines signatures. (I and J) mRNA levels (I) and protein concentrations (J) of four key myokines. (K and L) Representative IHC staining (K) and quantifications (L) of RAB27A. (M) EV secretion concentrations and particle size distributions. (N and O) Representative images (N) of Masson's staining, immunostaining of COL-1 and OCN, and TRAP staining and subsequent quantifications (O). (P) Biomechanical 3-point bending test parameters. (Q and R) Representative Micro-CT reconstructions (Q) and quantifications (R) of the harvested mice femurs. n = 14 biologically independent animals per cohort. Data are represented as mean ± SD. Statistical significance was determined utilizing one-way ANOVA followed by Tukey's post hoc test or the Kruskal-Wallis test followed by Dunn's multiple comparisons test. Exact p values are indicated within the respective panels.

1. Lu T, Xie Y, Wang Y, Lin X, Cai X, Zhang Y, et al. Protein restriction reprograms the multi-organ proteomic landscape of mouse aging. Cell. 2025;188(25):7309–26.e20. doi: 10.1016/j.cell.2025.10.004
2. Suryadevara V, Farzad N, Yang M, Xu K, Tsankov A, Thompson RC, et al. Charting human cellular senescence in aging and disease. Cell. 2026;189(12):3501–5. doi: 10.1016/j.cell.2026.05.028
3. Bossio S, Russa D, Rago V, Di Dio M, Aversa A, Perri A. Inflammaging: Immune-Metabolic Crosstalk Between the Prostate-Testis and Musculoskeletal System. Int J Mol Sci. 2026;27(8). doi: 10.3390/ijms27083612
4. Hou Y, Zeng Z, He S, He L, Liu K, Tang W, et al. Immunosenescence and inflammaging: from pathological hallmarks to rejuvenation strategies. J Gerontol A Biol Sci Med Sci. 2026;81(6). doi: 10.1093/gerona/glag108
5. Bieri G, Pratt KJB, Fuseya Y, Aghayev T, Sucharov J, Horowitz AM, et al. Liver exerkine reverses aging- and Alzheimer's-related memory loss via vasculature. Cell. 2026;189(5):1499–516.e25. doi: 10.1016/j.cell.2026.01.024
6. Zhao H, Liao M, Huo R, He T, Tian H, Li Z, et al. Restoring circadian rhythms in the hypothalamic paraventricular nucleus reverses aging biomarkers and extends lifespan in male mice. Cell. 2026;189(7):2007–23.e20. doi: 10.1016/j.cell.2026.01.016
7. Kroemer G, Maier AB, Cuervo AM, Gladyshev VN, Ferrucci L, Gorbunova V, et al. From geroscience to precision geromedicine: Understanding and managing aging. Cell. 2025;188(8):2043–62. doi: 10.1016/j.cell.2025.03.011
8. Aamir SW, Huang JW, Qadeer A, Alzahrani KJ, Alsharif KF, Alzahrani FM, et al. Extracellular Vesicles as Key SASP Carriers Driving Cellular Senescence, Inflammaging, and Therapeutic Opportunities in Aging and Age-Related Diseases. Aging Dis. 2026. doi: 10.14336/ad.2026.0134
9. Vints WAJ, Gökçe E, Langeard A, Pavlova I, Çevik Ö S, Ziaaldini MM, et al. Investigating the mediating effect of myokines on exercise-induced cognitive changes in older adults: A living systematic review and meta-analysis. Neurosci Biobehav Rev. 2025;178:106381. doi: 10.1016/j.neubiorev.2025.106381
10. Xu M, Liu X. Cisplatin-Induced Skeletal Muscle Atrophy: Biomolecular Mechanisms and the Protective Role of Exercise-Induced Myokines. Biomolecules. 2025;15(11). doi: 10.3390/biom15111495
11. Xue M, Liao C, Liu Y, Tian W, Liao L. Myokines in Aging: A Multi-Organ Network Perspective. Aging Dis. 2025. doi: 10.14336/ad.2025.1040
12. Liu M, Wang Y, Shi W, Yang C, Wang Q, Chen J, et al. PCDH7 as the key gene related to the co-occurrence of sarcopenia and osteoporosis. Front Genet. 2023;14:1163162. doi: 10.3389/fgene.2023.1163162
13. Farhana F, Sultana MA, Hia RA, Hegde V. Postmenopausal sarcopenia and Alzheimer's disease: The interplay of mitochondria, insulin resistance, and myokines. Neurosci Biobehav Rev. 2026;180:106501. doi: 10.1016/j.neubiorev.2025.106501
14. Gao S, Li N, Qi L, Li X, Zhang J, Zhang Z, et al. Myokines and osteokines in aging-related degenerative diseases: Regulatory networks in the muscle-bone-brain axis. Cytokine Growth Factor Rev. 2025;86:17–28. doi: 10.1016/j.cytogfr.2025.09.001

15. Hoseini R, Hoseini Z, Heydarpour B, Faraji M. A systematic review of molecular signaling in the muscle-brain-gut axis: exercise-induced myokines and microbial metabolites as key mediators. Mol Biol Rep. 2026;53(1). doi: 10.1007/s11033-026-12035-y
16. Lee H, Lim Y. Can Myokines Serve as Supporters of Muscle-Brain Connectivity in Obesity and Type 2 Diabetes? Potential of Exercise and Nutrition Interventions. Nutrients. 2025;17(22). doi: 10.3390/nu17223615
17. Maniscalco M, Fuschillo S, Ambrosino P, Candia C, di Domenico A, Lombardi C, et al. Skeletal muscle dysfunction in COPD: miRNAs, myokines and exercise. ERJ Open Res. 2026;12(3). doi: 10.1183/23120541.00887-2025
18. Zhang Y, Qiu Y. Exercise-Induced Myokines in Obesity-Related Metabolic Disorders and Cardiovascular Protection: A Narrative Review. Sports (Basel). 2026;14(5). doi: 10.3390/sports14050212
19. Liu Y, Zhou R, Guo Y, Hu B, Xie L, An Y, et al. Muscle-derived small extracellular vesicles induce liver fibrosis during overtraining. Cell Metab. 2025;37(4):824–41.e8. doi: 10.1016/j.cmet.2024.12.005
20. Xenos D, Mancinetti F, Mecocci P, Boccardi V. The muscle-brain axis in type 2 diabetes: Molecular pathways linking sarcopenia and cognitive decline. Ageing Res Rev. 2026;113:102955. doi: 10.1016/j.arr.2025.102955
21. Mori K, Imai SI. Muscle-derived Mimecan regulates hypothalamus-brown adipose tissue communication and promotes health and lifespan in mice. Cell Metab. 2026. doi: 10.1016/j.cmet.2026.04.003
22. Maki Y, Matsuse H, Hashida R, Matsukuma N, Tajima H, Baba E, et al. Matched Metabolic Stress Preserves Myokine Responses Regardless of Mechanical Load: A Randomized, Controlled Crossover Trial. Metabolites. 2025;15(10). doi: 10.3390/metabo15100641
23. Huang Y, Hu B, Liu Y, Xie LQ, Dai Y, An YZ, et al. Excessive vigorous exercise impairs cognitive function through a muscle-derived mitochondrial pretender. Cell Metab. 2026;38(2):281–97.e11. doi: 10.1016/j.cmet.2025.11.002
24. Tan SSL, Garg V, Dhiman A, Bansal N, Conway P. Inflammaging and the role of micronutrients as immunomodulators: a pathway to healthy aging. Immun Ageing. 2026. doi: 10.1186/s12979-026-00569-5
25. Zeidan RS, Shirali AS, Reinhard S, Picca A, Vial P, Pruinelli L, et al. Inflammaging: From Mechanisms to Clinical Implications and Targeted Interventions. Aging Dis. 2026. doi: 10.14336/ad.2025.1557
26. Liu M, Han Y, Wang J, Zhu Y, Zhang Y, Chu Q, et al. Skeletal muscle-derived IL-33 mediates muscle-to-bone crosstalk and regulates bone metabolism via CD8(+) T cell-secreted CCL5. EBioMedicine. 2025;122:106024. doi: 10.1016/j.ebiom.2025.106024
27. Alameen AAM, Al-Kuraishy HM, Abdelaziz AM, Batiha GE. Repurposing niclosamide to mitigate inflammaging: a review of multi-target mechanisms in cellular senescence and age-related decline. Inflamm Res. 2026;75(1). doi: 10.1007/s00011-026-02293-8
28. Liu M, Fu X, Yu D, Li M, Pan Y, Yang C, et al. Mapping the causal associations of cytokines with sarcopenia and aging traits: Evidence from bidirectional Mendelian

randomization. J Cachexia Sarcopenia Muscle. 2024;15(3):1121–33. doi: 10.1002/jcsm.13456
29. Liu M, Wang J, Han Y, Fu X, Pan Y, Yang C, et al. Comprehensive landscapes of the causal network between immunity and sarcopenia. Front Immunol. 2024;15:1443885. doi: 10.3389/fimmu.2024.1443885
30. Shao X, Zhang P, Fan Z, Lin J, Chen X, Liu N, et al. Atrophic Skeletal Muscle-Derived Extracellular Vesicles Transfer miR-125a-5p to Inhibit Bone Formation in Osteoporosis during Aging. Adv Sci (Weinh). 2026;13(25):e15362. doi: 10.1002/advs.202515362
31. Alotaibi MO, Al-Kuraishy HM, Fahad EH, Abdelaziz AM, El-Saber Batiha G. Targeting inflammaging in Alzheimer's disease: molecular pathways and emerging pharmacotherapies. Inflammopharmacology. 2026. doi: 10.1007/s10787-026-02281-8
32. Bautista J, López-Cortés A. Mitochondrial drivers of stem cell aging and inflammaging. NPJ Aging. 2026. doi: 10.1038/s41514-026-00422-5
33. Lu JY, Tu WB, Ma S, Ma Z, Imaz-Rosshandler I, Weng M, et al. Mesenchymal drift: A convergent framework for the hallmarks of aging. Cell. 2026;189(11):3184–213. doi: 10.1016/j.cell.2026.04.020
34. de Lima Camillo LP. Inhibition of mesenchymal drift as a strategy for rejuvenation. Front Pharmacol. 2025;16:1715559. doi: 10.3389/fphar.2025.1715559
35. Lu JY, Tu WB, Li R, Weng M, Sanketi BD, Yuan B, et al. Prevalent mesenchymal drift in aging and disease is reversed by partial reprogramming. Cell. 2025;188(21):5895–911.e17. doi: 10.1016/j.cell.2025.07.031
36. Judson RN, Low M, Eisner C, Rossi FM. Isolation, Culture, and Differentiation of Fibro/Adipogenic Progenitors (FAPs) from Skeletal Muscle. Methods Mol Biol. 2017;1668:93–103. doi: 10.1007/978-1-4939-7283-8_7
37. Raue U, Trappe TA, Estrem ST, Qian HR, Helvering LM, Smith RC, et al. Transcriptome signature of resistance exercise adaptations: mixed muscle and fiber type specific profiles in young and old adults. J Appl Physiol (1985). 2012;112(10):1625–36. doi: 10.1152/japplphysiol.00435.2011
38. Robinson MM, Dasari S, Konopka AR, Johnson ML, Manjunatha S, Esponda RR, et al. Enhanced Protein Translation Underlies Improved Metabolic and Physical Adaptations to Different Exercise Training Modes in Young and Old Humans. Cell Metab. 2017;25(3):581–92. doi: 10.1016/j.cmet.2017.02.009
39. Michie KL, Kunz HE, Dasari S, Lanza IR. The Influence of Aging on the Unfolded Protein Response in Human Skeletal Muscle at Rest and after Acute Exercise. Med Sci Sports Exerc. 2024;56(11):2135–45. doi: 10.1249/mss.0000000000003508
40. Kurochkina NS, Orlova MA, Vigovskiy MA, Zgoda VG, Vepkhvadze TF, Vavilov NE, et al. Age-related changes in human skeletal muscle transcriptome and proteome are more affected by chronic inflammation and physical inactivity than primary aging. Aging Cell. 2024;23(4):e14098. doi: 10.1111/acel.14098
41. Perez K, Ciotlos S, McGirr J, Limbad C, Doi R, Nederveen JP, et al. Single nuclei profiling identifies cell specific markers of skeletal muscle aging, frailty, and senescence. Aging (Albany NY). 2022;14(23):9393–422. doi: 10.18632/aging.204435

42. Barter MJ, Cheung K, Falk J, Panagiotopoulos AC, Cosimini C, O'Brien S, et al. Dynamic chromatin accessibility landscape changes following interleukin-1 stimulation. Epigenetics. 2021;16(1):106–19. doi: 10.1080/15592294.2020.1789266
43. Rubenstein AB, Hinkley JM, Nair VD, Nudelman G, Standley RA, Yi F, et al. Skeletal muscle transcriptome response to a bout of endurance exercise in physically active and sedentary older adults. Am J Physiol Endocrinol Metab. 2022;322(3):E260–e77. doi: 10.1152/ajpendo.00378.2021
44. Kang PB, Kho AT, Sanoudou D, Haslett JN, Dow CP, Han M, et al. Variations in gene expression among different types of human skeletal muscle. Muscle Nerve. 2005;32(4):483–91. doi: 10.1002/mus.20356
45. Schaiter A, Hentschel A, Kleefeld F, Schuld J, Umathum V, Procida-Kowalski T, et al. Molecular composition of skeletal muscle in infants and adults: a comparative proteomic and transcriptomic study. Sci Rep. 2024;14(1):22965. doi: 10.1038/s41598-024-74913-4
46. Wang H, Chen Y, Wang T, Ye X, Zhang X, Xie Y, et al. EV-Mediated Intracardiac Crosstalk Mitigates Doxorubicin-Induced Cardiotoxicity. Circ Res. 2026;138(10):e327827. doi: 10.1161/circresaha.125.327827
47. Singh N, Pathak Z, Kumar H. Rab27a-mediated extracellular vesicle release drives astrocytic CSPG secretion and glial scarring in spinal cord injury. Biomater Adv. 2025;176:214357. doi: 10.1016/j.bioadv.2025.214357
48. Sahu SK, Reddy P, Lu J, Shao Y, Wang C, Tsuji M, et al. Targeted partial reprogramming of age-associated cell states improves markers of health in mouse models of aging. Sci Transl Med. 2024;16(764):eadg1777. doi: 10.1126/scitranslmed.adg1777
49. Liu YW, Zou JT, Gong JS, Jin L, Cao J, He ZH, et al. Local delivery of OSK factors enables partial cellular reprogramming to mitigate osteoarthritis and cartilage fibrosis. Exp Mol Med. 2026;58(3):782–97. doi: 10.1038/s12276-026-01662-x
50. Berdugo-Vega G, Sierra C, Astori S, Calati V, Orsat J, Scoglio MJ, et al. Cognitive rejuvenation through partial reprogramming of engram cells. Neuron. 2026;114(6):1102–16.e7. doi: 10.1016/j.neuron.2025.11.028
51. Li Y, Li C, Zhou Q, Liu X, Qiao Y, Xie T, et al. Multiomics and cellular senescence profiling of aging human skeletal muscle uncovers Maraviroc as a senotherapeutic approach for sarcopenia. Nat Commun. 2025;16(1):6207. doi: 10.1038/s41467-025-61403-y
52. Zhang C, Bai Y, Yin Q, Li J, Huang K, Qiu M. Hepatocyte-specific partial cellular reprogramming via selective OSK mRNA lipid nanoparticle attenuates liver fibrosis. J Control Release. 2026;390:114569. doi: 10.1016/j.jconrel.2025.114569
53. Matsuo-Tani A, Matsumoto M, Hiu T, Kamiya M, Geng L, Takayama R, et al. Targeted Delivery of VEGF-siRNA to Glioblastoma Using Orientation-Controlled Anti-PD-L1 Antibody-Modified Lipid Nanoparticles. Pharmaceutics. 2025;17(10). doi: 10.3390/pharmaceutics17101298
54. Yao Y, Luo Y, Liang X, Zhong L, Wang Y, Hong Z, et al. The role of oxidative stress-mediated fibro-adipogenic progenitor senescence in skeletal muscle regeneration and repair. Stem Cell Res Ther. 2025;16(1):104. doi: 10.1186/s13287-025-04242-4

55. Molina T, Fabre P, Garcia P, Kim TY, Gurlekian Z, Tellier L, et al. Fibroadipogenic progenitor-secreted prostaglandin E2 coordinates stem cell fate via autocrine and paracrine crosstalk in healthy and dystrophic muscle. Cell Death Differ. 2026. doi: 10.1038/s41418-026-01762-1
56. Ambrosio F, Artyomov MN, Austad SN, Barzilai N, Belmonte JCI, Belsky DW, et al. Past, present and future perspectives on the science of aging. Nat Aging. 2026;6(1):6–22. doi: 10.1038/s43587-025-01046-2
57. Zubova A, Pietrocola F, Morsli S. Immunological consequences of senescence in physiology and pathology. J Transl Med. 2026;24(1). doi: 10.1186/s12967-026-08335-3
58. Hussain A, Tatar M, Gong R. Molecular mechanisms and recent advances in cellular senescence. Cell Biosci. 2026. doi: 10.1186/s13578-026-01596-x
59. Deng Q, Huang J, Wang C, Liang J. Exercise-Induced Exerkines Modulate Autophagy: Implications for Interorgan Crosstalk in the Hallmarks of Ageing. Int J Mol Sci. 2026;27(6). doi: 10.3390/ijms27062746
60. de Vries GM, De Ridder W, Baets J. Ageing-Associated Dysregulation of Myogenic Differentiation in Inclusion Body Myositis. J Cachexia Sarcopenia Muscle. 2026;17(3):e70301. doi: 10.1002/jcsm.70301
61. Cui X, Liu H, Liu Y, Yu Z, Wang D, Wei W, et al. The role and mechanisms of myokines in sarcopenia: new intervention strategies for the challenges of aging. Front Med (Lausanne). 2025;12:1665708. doi: 10.3389/fmed.2025.1665708
62. Chuang CL, Rai M, Demontis F. Muscle-to-CNS signaling in physiological homeostasis, aging, and disease. Trends Mol Med. 2026. doi: 10.1016/j.molmed.2026.03.006
63. Zhang B, Chen Y, Chen Q, Zhang H. Exosomal miRNAs in muscle-bone crosstalk: Mechanistic links, exercise modulation and implications for sarcopenia, osteoporosis and osteosarcopenia. Metabolism. 2025;170:156333. doi: 10.1016/j.metabol.2025.156333
64. Li G, Qi M, Wang Y, Liang S, Xu H. Molecular communication from bone to skeletal muscle: an overview. Front Cell Dev Biol. 2025;13:1715009. doi: 10.3389/fcell.2025.1715009
65. Kaji H. Bone-muscle interactions. Osteoporos Sarcopenia. 2025;11(2 Suppl):32–9. doi: 10.1016/j.afos.2025.04.001
66. Boss-Kennedy A, Kim D, Barai P, Maldonado C, Reyes-Ordoñez A, Chen J. Muscle cell-derived Ccl8 is a negative regulator of skeletal muscle regeneration. Faseb j. 2024;38(14):e23841. doi: 10.1096/fj.202400184R
67. Mao Y, Jin Z, Yang J, Xu D, Zhao L, Kiram A, et al. Muscle-bone cross-talk through the FNIP1-TFEB-IGF2 axis is associated with bone metabolism in human and mouse. Sci Transl Med. 2024;16(750):eadk9811. doi: 10.1126/scitranslmed.adk9811
68. Ma S, Xing X, Huang H, Gao X, Xu X, Yang J, et al. Skeletal muscle-derived extracellular vesicles transport glycolytic enzymes to mediate muscle-to-bone crosstalk. Cell Metab. 2023;35(11):2028–43.e7. doi: 10.1016/j.cmet.2023.10.013
69. Sorokina MY, Ivanova OA, Kostareva AA, Dmitrieva RI. Fibro-Adipogenic Progenitor Cell Alterations in Skeletal Muscle: Pathological Dysfunction or Adaptive Reprogramming? Int J Mol Sci. 2026;27(11). doi: 10.3390/ijms27115016

70. Nelke C, Sanchez-Dal Cin J, Dallevet CA, Park JS, Kinold JC, Schroeter CB, et al. Inflammation reprograms fibro-adipogenic progenitors to sustain immunopathogenic niches in myositis. Cell Death Dis. 2026;17(1). doi: 10.1038/s41419-026-08966-w
71. Puri D, Wagner W. Epigenetic rejuvenation by partial reprogramming. Bioessays. 2023;45(4):e2200208. doi: 10.1002/bies.202200208
72. Olova N, Simpson DJ, Marioni RE, Chandra T. Partial reprogramming induces a steady decline in epigenetic age before loss of somatic identity. Aging Cell. 2019;18(1):e12877. doi: 10.1111/acel.12877
73. Nakatsukasa Y, Yamada Y, Yamada Y. Research of in vivo reprogramming toward clinical applications in regenerative medicine: A concise review. Regen Ther. 2025;28:12–9. doi: 10.1016/j.reth.2024.11.008

Supplementary Files

This is a list of supplementary files associated with this preprint. Click to download.

- SupplementaryFigures.docx
- STables.xlsx